

AD-A112 370

OHIO STATE UNIV COLUMBUS ELECTROSCIENCE LAB

F/6 20/3

A UNIFORM ASYMPTOTIC RESULT FOR THE SCATTERING OF PLANE WAVES BY--ETC(U)

N62269-74-C-0708

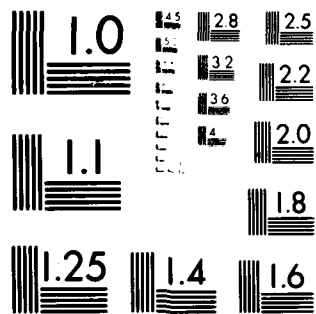
UNCLASSIFIED

ESL-3973-1

NL

$$\|u\|_{\dot{W}^{1,2}_0(\Omega)}$$

END  
DATE  
FILMED  
4 -82  
DTIC

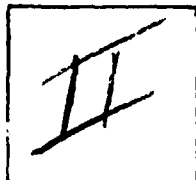


MICROCOPY RESOLUTION TEST CHART  
NATIONAL BUREAU OF STANDARDS-1963-A

PHOTOGRAPH THIS SHEET

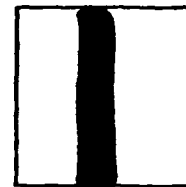
A118  
370

DTIC ACCESSION NUMBER



LEVEL

Ohio State Univ., Columbus  
ElectroScience Lab.



INVENTORY

*A Uniform Asymptotic Result for the Scattering  
of Plane Waves by A Circular Cylinder.*

DOCUMENT IDENTIFICATION

Mar. 76

Contract N62269-74-C-0788 Rpt. No. ESL-3973-1

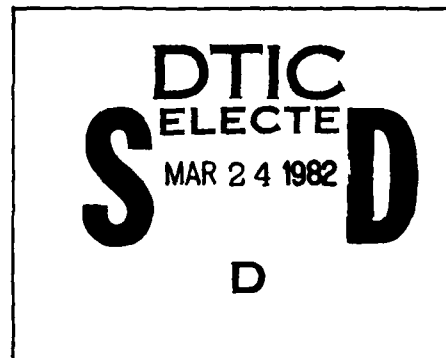
DISTRIBUTION STATEMENT A

Approved for public release  
Distribution Unlimited

DISTRIBUTION STATEMENT

ACCESSION FOR	
NTIS	GRA&I <input checked="" type="checkbox"/>
DTIC	TAB <input type="checkbox"/>
UNANNOUNCED	<input type="checkbox"/>
JUSTIFICATION	
Per Ltr. on file	
EL-88, Acc # 82-0024(6)	
BY Thul (d) 26 Jan 82	
DISTRIBUTION /	
AVAILABILITY CODES	
DIST	AVAIL AND/OR SPECIAL
A	

DISTRIBUTION STAMP



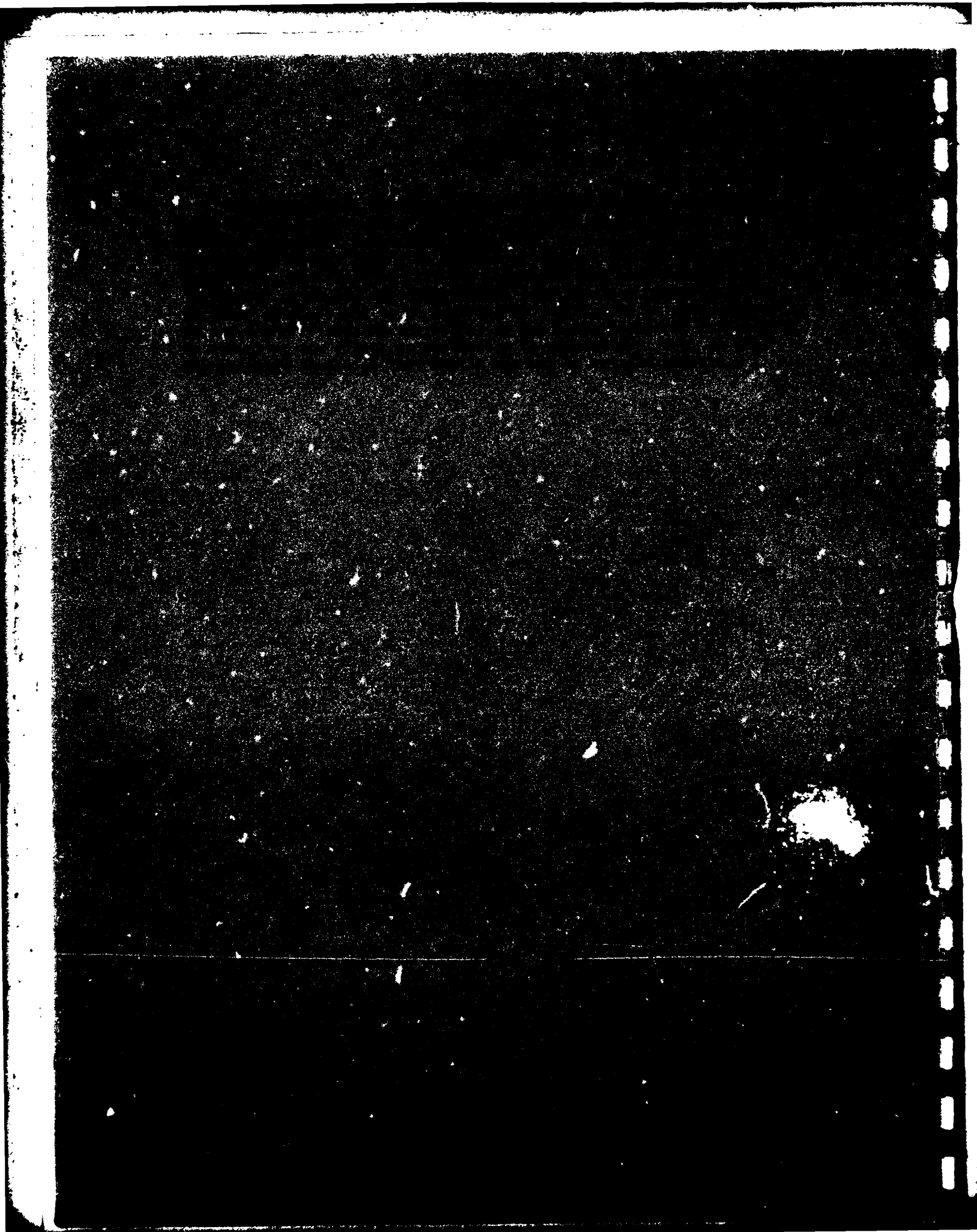
DATE ACCESSIONED

82 03 08 149

DATE RECEIVED IN DTIC

PHOTOGRAPH THIS SHEET AND RETURN TO DTIC-DDA-2

AD A112370



SECURITY CLASSIFICATION OF THIS PAGE (When Data Entered)

DD FORM 1 JAN 73 1473 EDITION OF 1 NOV 65 IS OBSOLETE

~~UNCLASSIFIED~~  
SECURITY CLASSIFICATION OF THIS PAGE (When Data Entered)

UNCLASSIFIED

SECURITY CLASSIFICATION OF THIS PAGE(When Data Entered)

20.

and lit zones, respectively. The accuracy of this transition solution is confirmed by numerical comparison with the results obtained via an exact solution for the same canonical problem. The transition solution is in terms of well tabulated functions, and it is simple and accurate for engineering applications (e.g., in determining the fields of wing or tail mounted aircraft antennas).

UNCLASSIFIED

SECURITY CLASSIFICATION OF THIS PAGE(When Data Entered)

## TABLE OF CONTENTS

	Page
I. INTRODUCTION	1
II. ANALYTICAL DETAILS	5
A. Transition Region - Shadow Zone	8
B. Transition Region - Illuminated Zone	25
III. NUMERICAL RESULTS	33
IV. SUMMARY AND DISCUSSION	56
REFERENCES	58
APPENDIX	60



# LIST OF ILLUSTRATIONS

Figure		Page
1	Rays associated with the plane wave scattering by a smooth convex cylinder	2
2	Geometry of the canonical problem	5
3	Contours of integration for $I_1$ and $I_2$	9
4	Contours of integration for Bessel functions	11
5	Location of $\beta_s$ , $\beta_p$ and SDP for the shadow region analysis	12
6	Transition region correction factor $F(kLa)$ (the positive branch of $\sqrt{kLa}$ is taken)	15
7	Geometrical parameters for the shadow region	16
8(a)	Plot of $e^{-i\pi/4} p^*(\xi)$ versus $\xi$ based on Logan's tabulated data [9] for $p(\xi)$	18
8(b)	Plot of $e^{-i\pi/4} q^*(\xi)$ versus $\xi$ based on Logan's tabulated data [9] for $q(\xi)$	19
9	Location of $\beta_s$ , $\beta_p$ and SDP for the lit region	21
10	Geometrical parameters for the lit region	22
11	Reflected ray system	26
12(a)	Field surrounding a circular cylinder illuminated by a $TE_z$ plane wave. Calculations based on GTD and the transition solution	34
12(b)	Comparison of the composite GTD plus transition solution of Fig. 12(a) with the exact solution	35
13(a)	Field surrounding a circular cylinder illuminated by a $TE_z$ plane wave. Calculations based on GTD and the transition solution	36
13(b)	Comparison of the composite GTD plus transition solution of Fig. 13(a) with the exact solution	37
14(a)	Field surrounding a circular cylinder illuminated by a $TE_z$ plane wave. Calculations based on GTD and the transition solution	38

# LIST OF ILLUSTRATIONS (continued)

Figure		Page
14(b)	Comparison of the composite GTD plus transition solution of Fig. 14(a) with the exact solution	39
15(a)	Field surrounding a circular cylinder illuminated by a $TE_z$ plane wave. Calculations based on GTD and the transition solution	40
15(b)	Comparison of the composite GTD plus transition solution of Fig. 15(a) with the exact solution	41
16(a)	Field surrounding a circular cylinder illuminated by a $TE_z$ plane wave. Calculations based on GTD and the transition solution	42
16(b)	Comparison of the composite GTD plus transition solution of Fig. 16(a) with the exact solution	43
17(a)	Field surrounding a circular cylinder illuminated by a $TE_z$ plane wave. Calculations based on GTD and the transition solution	44
17(b)	Comparison of the composite GTD plus transition solution of Fig. 17(a) with the exact solution	45
18(a)	Field surrounding a circular cylinder illuminated by a $TE_z$ plane wave. Calculations based on GTD and the transition solution	46
18(b)	Comparison of the composite GTD plus transition solution of Fig. 18(a) with the exact solution	47
19(a)	Field surrounding a circular cylinder illuminated by a $TE_z$ plane wave. Calculations based on GTD and the transition solution	48
19(b)	Comparison of the composite GTD plus transition solution of Fig. 19(a) with the exact solution	49
20(a)	Field surrounding a circular cylinder illuminated by a $TE_z$ plane wave. Calculations based on GTD and the transition solution	50
20(b)	Comparison of the composite GTD plus transition solution of Fig. 20(a) with the exact solution	51

# LIST OF ILLUSTRATIONS (continued)

Figure		Page
21(a)	Field surrounding a circular cylinder illuminated by a $TM_z$ plane wave. Calculations based on GTD and the transition solution	52
21(b)	Comparison of the composite GTD plus transition solution of Fig. 21(a) with the exact solution	53
22(a)	Field surrounding a circular cylinder illuminated by a $TM_z$ plane wave. Calculations based on GTD and the transition solution	54
22(b)	Comparison of the composite GTD plus transition solution of Fig. 22(a) with the exact solution	55
A-I	Contour of integration $C_V$	61
A-II	Reflected ray geometry	62

## I. INTRODUCTION

When the geometrical theory of diffraction (GTD) [1,2] is employed to analyze the problem of high frequency plane wave scattering by smooth convex surfaces, a modification of this method is required for analyzing the fields in the vicinity of the shadow boundaries associated with this problem. This modification of the GTD forms the subject of the present paper.

In the GTD analysis of the diffraction of waves by a smooth convex cylinder [3], the total field exterior to it is associated in a simple manner with the usual incident and reflected rays of geometrical optics together with the surface diffracted rays introduced by Keller. The geometric optical rays are present only in the lit (or illuminated) region, so that the surface diffracted rays alone account for the field in the shadow region (these surface diffracted rays are also present in the illuminated region if the cylinder cross-section is closed). However, pure ray optical field descriptions fail at and near shadow boundaries, and at caustics of ray systems; consequently, the GTD ray solution for the problem illustrated in Fig. 1 is valid in regions I and III, but it fails in regions II, IV, V, and VI. Region II constitutes the penumbral or transition region adjacent to the shadow boundary (SB). The angular extent of this transition region is

$$0 \left[ 2 \left( \frac{2}{k \rho_g(Q_1)} \right)^{1/3} \right] \text{ where } k \text{ refers to the wavenumber of the}$$

surrounding medium which is assumed here to be free space, and  $\rho_g(Q_1)$  is the radius of curvature of the cylinder at the point of grazing incidence, i.e., at  $Q_1$ . Regions IV, V, and VI are usually referred to as the surface or caustic boundary layer regions. In shadow regions IV and V, the surface of the obstacle is a caustic of the surface diffracted rays; whereas, region VI is in the neighborhood of  $Q_1$  which is a caustic of the reflected ray for grazing incidence. The mathematical representations for the field within the transition regions, the surface boundary layer regions, and also their common regions of overlap are complicated by the fact that they must change rapidly but smoothly from one form to another across these regions.

It is evident that the usefulness and versatility of the GTD solution is further enhanced if it can be modified within the region where it fails; such modifications may be achieved by introducing uniform solutions which not only remain valid in one or more of these regions, but which reduce to the conventional GTD results exterior to these regions.

The development of a simple, uniform solution which remains valid in region II that is exterior to the surface boundary layer is considered in this paper. This work is motivated by the need

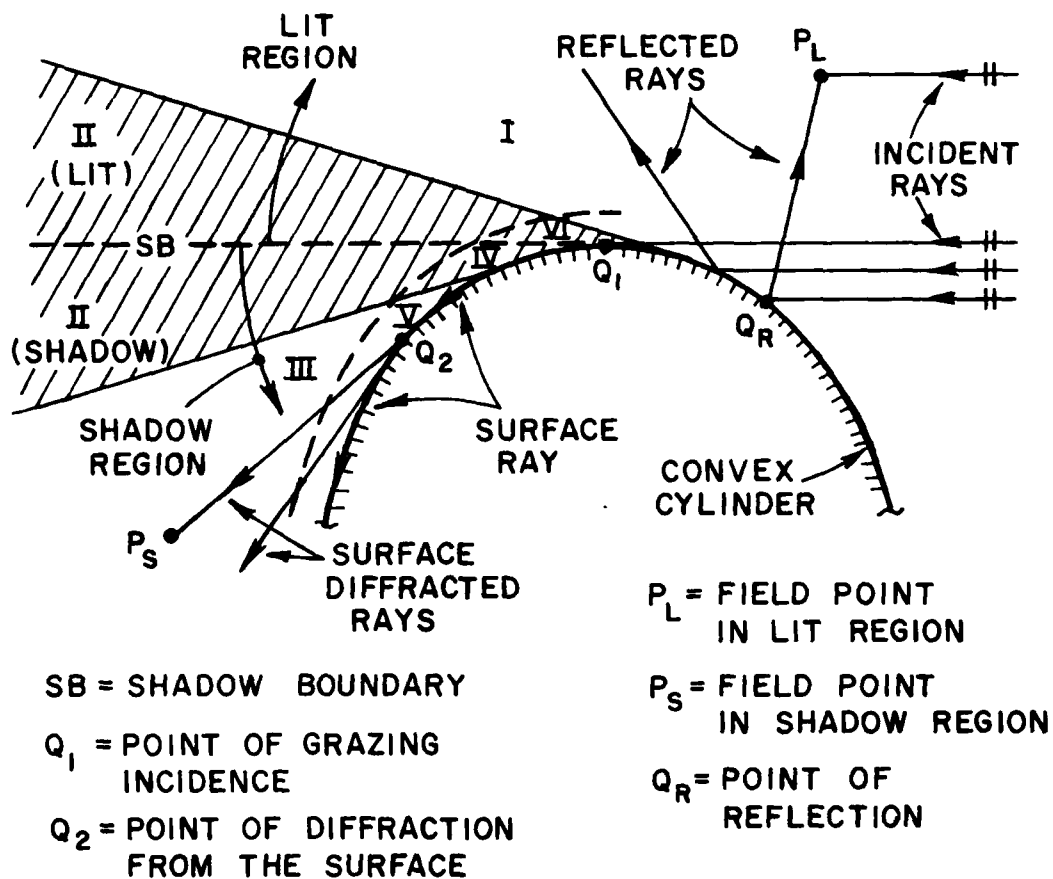


Fig. 1. Rays associated with the plane wave scattering by a smooth convex cylinder.

to analyze the radiation patterns of antennas mounted on the wings or tails of aircraft [4,5]. The radiation patterns of such antennas are significantly affected due to shadowing by the aircraft fuselage surface which is generally smooth and convex shaped. In many such wing or tail mounted aircraft antenna configurations, a knowledge of the field in the transition (or penumbral) region is essential for the purposes of antenna design. One can develop a solution for the transition region via an asymptotic high frequency analysis of a canonical problem which closely models the local geometry of the convex cylinder at  $Q_1$ .

In this paper, the canonical problem of plane wave scattering by a perfectly-conducting circular cylinder is solved by introducing certain asymptotic approximations, which are based on physical considerations, to obtain a uniform asymptotic result that is valid in the transition region exterior to the surface boundary layer. This uniform result yields a finite, continuous solution for the total field across the SB within the transition region. Exterior to this transition region, it reduces to the usual GTD solution in terms of surface diffracted and geometric optical ray fields for the shadow and lit zones, respectively. Furthermore, this result is in a form which is simple and convenient for engineering applications. Upon invoking the principle of the local character of the high frequency fields in the penumbra, one can systematically modify the uniform result for the circular cylinder to treat the electromagnetic scattering by arbitrary, smooth convex surfaces for both two- and three-dimensional problems. These extensions will be presented in detail in a separate paper.

The analysis of the canonical problem is indicated in section II. Numerical results based on this uniform-GTD analysis are compared in section III against the results obtained from an exact eigenfunction series solution for the same canonical problem where, it is seen that the present uniform result is accurate not only within, but also exterior to the transition region. A summary and discussion follows in section IV. Before proceeding with the analysis, the present work will be compared with the work of others on this subject.

The problem of asymptotically estimating the fields within the transition regions associated with the diffraction of waves by smooth, convex surfaces has had long standing interest, especially in connection with the theory of radio wave propagation around the earth. The fundamental work of Fock on this subject [6] appears to be the most significant; in particular, his analysis of the fields near a shadow boundary and within the Fresnel region of a diffracting spherical surface [7] is of direct relevance to the problem considered here. Other notable works which are also directly related to the present analysis are due to Wait and Conda [8], Logan and Yee [9,10], and Ivanov [11]. An extensive bibliography on various aspects of the problem of diffraction by a smooth, convex surface may be found in the papers by Logan [9,10], and Borovikov and Kimber [12]. Indeed, the present work draws upon the earlier, important contributions of Fock and Logan.

In Fock's analysis [7], the wave equation within the transition region is solved approximately via the method of parabolic equations; this solution is initially expressed in terms of a canonical integral introduced earlier by Fock [13a,b]. For observation points near the shadow boundary and the diffracting surface (but outside the surface boundary layer), this canonical integral is reduced by Fock to integrals which are functions of only a single parameter; in particular, the solution is expressed in terms of a Fresnel integral and a Pekeris-type integral [9,10], both of which are well tabulated.

Wait and Conda [8] analyze the field in the transition region scattered by a circular cylinder via an asymptotic evaluation of the radiation integral which employs the well-known Fock currents [13a] for this problem; their asymptotic solution near the shadow boundary is also given in terms of Fresnel and Pekeris integrals as done earlier by Fock [7]. In addition, the result given in [8] is valid not only near the surface (outside the surface boundary layer) as in [7], but also in the far zone. The analysis in [8] is an extension and generalization of the work of Goriainov [14].

The results in [7], [8], and [14] are quite accurate in the illuminated region very close to the SB, but in general they do not join smoothly with the geometrical optics field; whereas, the result presented here does reduce to the geometrical optics field in the illuminated region. Also, the present result is valid in both the near and far zone as in [8]; furthermore, exactly on the shadow boundary, it agrees with the results of [7], [8], and [14] which are accurate near the shadow boundary. Logan and Yee [10] give a result for the illuminated part of the transition region in terms of the canonical integral of Fock such that it reduces to the geometrical optics field far from the shadow boundary. This result appears to have been constructed by redefining certain parameters in Fock's canonical integral on an ad hoc basis.

Ivanov [11] analyzes the same canonical problem as in this paper via the method of parabolic equations; his solution which is valid in the transition and the surface boundary layer regions, and which reduces to the GTD solution outside the transition region, is also given in terms of an integral related to the canonical integral of Fock. The canonical Fock integral-type solutions [10,11] are complicated for numerical evaluation in the transition region except when the field point is either very close to the shadow boundary, or is on the surface; in these exceptional cases, they reduce to well tabulated integrals which are functions of only a single parameter.

On the other hand, using a somewhat less formal analytical procedure than the parabolic equation method employed in [7], [10], and [11], the present solution is given in terms of the well tabulated single parameter Fresnel and Pekeris integrals for the entire transition region (exterior to the surface boundary

layer). In this sense, the present result indicates a simplification over the results in [7], [10], and [11], respectively, for field points outside the surface boundary layer; furthermore, this simplification is achieved without any apparent loss of accuracy as confirmed by the numerical calculations in section III.

## II. ANALYTICAL DETAILS

An asymptotic high frequency analysis of the canonical problem of electromagnetic plane wave scattering by a perfectly-conducting circular cylinder in free space is presented in this section; both, the TE and the TM polarization cases are considered. The geometrical configuration of this canonical problem is illustrated in Fig. 2.

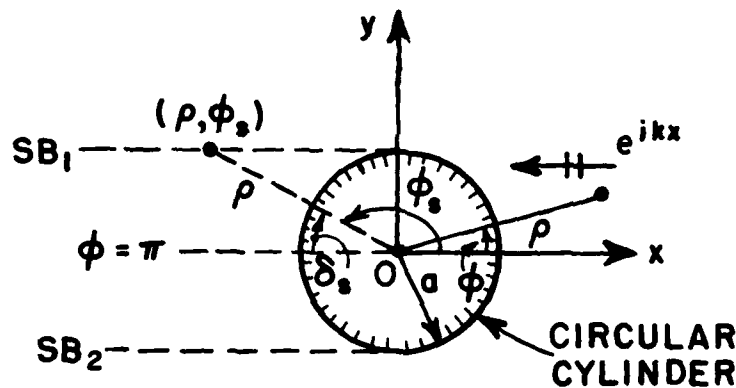


Fig. 2. Geometry of the canonical problem.

Let the incident plane wave field be denoted by  $U^i$ , and the scattered field by  $U^s$ ; then, the total field is  $U = U^i + U^s$  exterior to the cylinder. The total field  $U$  corresponds to a  $z$ -directed electric field if the excitation is  $TM_z$  polarized; whereas, it corresponds to a  $z$ -directed magnetic field if the excitation is  $TE_z$  polarized. The form of the incident field  $U^i$  is:

$$(1) \quad U^i = e^{ikx}.$$

The total field,  $U$  satisfies the reduced wave equation

$$(2) \quad (\nabla^2 + k^2) U = 0,$$



where  $\nabla^2$  is the usual 2-D Laplacian operator in cylindrical coordinates  $(\rho, \phi)$ . The scattered field  $U^s$  satisfies the Sommerfeld radiation condition for an  $e^{+i\omega t}$  time dependence (which is assumed and suppressed), and the total field  $U(\rho, \phi)$  satisfies the following boundary conditions on the cylinder:

$$(3) \quad Q \left[ U(\rho, \phi) \right] = 0, \text{ at } \rho = a; Q \equiv \begin{cases} 1, & \text{for the TM}_z \text{ case} \\ \frac{a}{\partial \rho}, & \text{for the TE}_z \text{ case.} \end{cases}$$

The solution to (2) subject to the radiation condition and (3) is [15]

$$(4a) \quad U = -i \int_{-\infty-i\epsilon}^{\infty-i\epsilon} dv \left[ J_v(k\rho) - \frac{Q J_v(ka)}{Q H_v^{(2)}(ka)} H_v^{(2)}(k\rho) \right] \frac{\cos v(\pi - |\phi|)}{\sin v\pi} e^{iv\frac{\pi}{2}},$$

or

$$(4b) \quad U = -\frac{i}{2} \int_{-\infty-i\epsilon}^{\infty-i\epsilon} dv \left[ H_v^{(1)}(k\rho) - \frac{Q H_v^{(1)}(ka)}{Q H_v^{(2)}(ka)} H_v^{(2)}(k\rho) \right] \frac{\cos v(\pi - |\phi|)}{\sin v\pi} e^{iv\frac{\pi}{2}},$$

with  $\epsilon > 0$ , and  $\epsilon \rightarrow 0$ . The quantities  $J_v, H_v^{(1)}, H_v^{(2)}$  are the usual cylinder Bessel and Hankel functions. It is noted that  $\text{Im}(v) < 0$  on the contour of integration in (4a) and (4b).

The above integral expressions for  $U$  may be rewritten by employing the decomposition

$$(5) \quad \cos v(\pi - |\phi|) = e^{-iv\pi} \cos v\phi + i e^{-iv|\phi|} \sin v\pi.$$

Thus, for large  $ka$  (i.e.,  $ka \gg 1$ ), one obtains

$$(6a) \quad U \approx \int_{-\infty-i\epsilon}^{\infty-i\epsilon} dv \left[ J_v(k\rho) - \frac{Q J_v(ka)}{Q H_v^{(2)}(ka)} H_v^{(2)}(k\rho) \right] e^{-iv[|\phi| - \frac{\pi}{2}]},$$

or

$$(6b) \quad U \approx \frac{1}{2} \int_{-\infty-i\epsilon}^{\infty+i\epsilon} dv \left[ H_v^{(1)}(k\rho) - \frac{Q H_v^{(1)}(ka)}{Q H_v^{(2)}(ka)} H_v^{(2)}(k\rho) \right] \cdot e^{-iv[|\phi| - \frac{\pi}{2}]},$$

with  $0 < |\phi| < \pi$ . In going from (4) to (6) via (5), the terms containing  $e^{iv\pi} \cos v\phi$  are discarded because they can be shown to correspond to the multiply encircling GTD surface ray modes which contribute negligibly for large  $ka$ . Within the transition region,  $v \sim 0$  ( $ka$ ) so that  $J_v(ka)$  and  $H_v^{(2)}(ka)$  become for large  $ka$ :

$$(7a) \quad J_v(ka) \approx \frac{1}{m\sqrt{\pi}} V(m^{-1}[v-ka]);$$

$$(7b) \quad H_v^{(2)}(ka) \approx \mp \frac{i}{m\sqrt{\pi}} W_1(m^{-1}[v-ka])$$

where  $m \equiv \left(\frac{ka}{2}\right)^{1/3}$ , and the quantities  $V$  and  $W_1$  are the Fock-type

Airy functions\* [9]. Introducing the change of variable  $\tau = m^{-1}[v-ka]$  now allows one to express (6) in terms of (7) as:

$$(8a) \quad U \approx m \int_{-\infty-i\epsilon}^{\infty+i\epsilon} d\tau \left[ J_{v(\tau)}(k\rho) + i \frac{\tilde{Q} V(\tau)}{\tilde{Q} W_2(\tau)} H_{v(\tau)}^{(2)}(k\rho) \right] \cdot e^{-iv(\tau)\psi},$$

---

\*  $W_{1,2}(\tau) \equiv \frac{1}{\sqrt{\pi}} \int_{\Gamma_{1,2}} e^{\tau t - t^3/3}$ ;  $2iV(\tau) \equiv W_1(\tau) - W_2(\tau)$ . The contour  $\Gamma_1$  runs from  $\infty e^{-i\frac{2\pi}{3}}$  to  $\infty - i\epsilon$ ; whereas,  $\Gamma_2$  is the complex conjugate of  $\Gamma_1$ .

or

$$(8b) \quad U \approx \frac{m}{2} \int_{-\infty - i\epsilon}^{\infty - i\epsilon} d\tau \left[ H_{\nu(\tau)}^{(1)}(k\rho) + \frac{\tilde{Q} W_1(\tau)}{Q W_2(\tau)} H_{\nu(\tau)}^{(2)}(k\rho) \right] e^{-i\nu(\tau)\psi},$$

with

$$(8c) \quad \tilde{Q} \approx \begin{cases} 1, & \text{for the TM}_z \text{ case} \\ \frac{\partial}{\partial \tau}, & \text{for the TE}_z \text{ case} \end{cases}.$$

Also,  $\nu(\tau) = ka + m\tau$ ,  $\psi \equiv |\phi| - \frac{\pi}{2}$ , and  $\text{Im}(\tau) < 0$  in the integrands of (8a) and (8b).

The integral representations for  $U$  in (8) will next be asymptotically approximated for the shadowed zone of the transition region in part A of this section; whereas, the asymptotic approximation for  $U$  in the illuminated zone of the transition region will follow in part B.

#### A. Transition Region - Shadow Zone

One begins by rewriting (8) in a manner analogous to that done by Fock [7] in the decomposition of a canonical integral representing the solution of his parabolic equation for the problem of diffraction by a sphere; namely,  $U$  is written as a superposition of two integrals, one being the integral in (8a) over the contour from  $0 - i\epsilon$  to  $\infty - i\epsilon$  (defined as contour  $C_2$ ), and the other being the integral in (8b) over the contour from  $-\infty - i\epsilon$  to  $0 - i\epsilon$  (defined as contour  $C_1$ ). Thus,

$$(9) \quad U \approx I_1 + I_2,$$

where

$$(10a) \quad I_1 \equiv m \int_{C_1 + C_2} J_{\nu(\tau)}(k\rho) e^{-i\nu(\tau)\psi} d\tau - \frac{m}{2} \int_{C_1} H_{\nu(\tau)}^{(2)}(k\rho) e^{-i\nu(\tau)\psi} d\tau$$

and

$$(10b) \quad I_2 \equiv \text{im} \int_{C_2} \frac{\tilde{Q} V(\tau)}{\tilde{Q} W_2(\tau)} H_{\nu(\tau)}^{(2)}(k\rho) e^{-iv(\tau)\psi} d\tau \\ + \frac{m}{2} \int_{C_1} \frac{\tilde{Q} W_1(\tau)}{\tilde{Q} W_2(\tau)} H_{\nu(\tau)}^{(2)}(k\rho) e^{-iv(\tau)\psi} d\tau.$$

The contours  $C_1$  and  $C_2$  are shown in Figs. 3(a) and 3(b), respectively. One notes that  $I_1$  is independent of the electrical properties of the cylinder; whereas,  $I_2$  is strongly dependent on these properties.

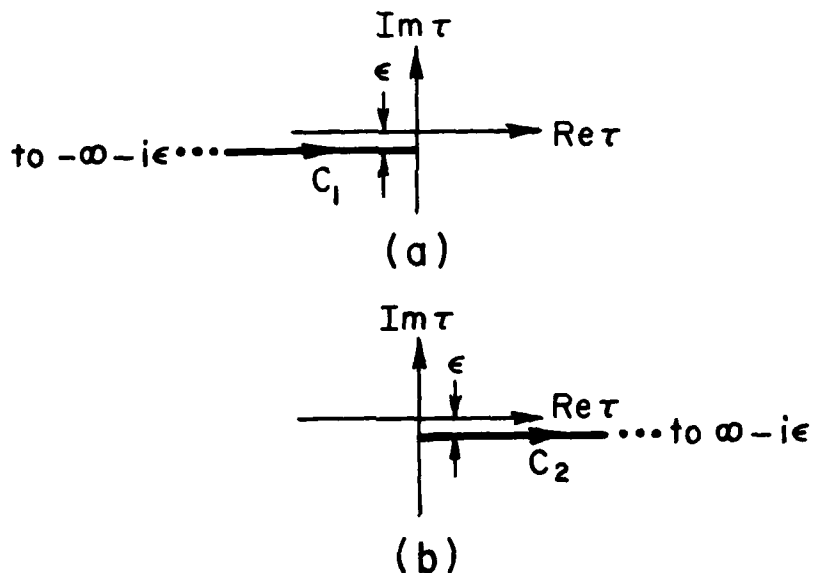


Fig. 3. Contours of integration for  $I_1$  and  $I_2$ .

For the sake of definiteness, the fields in the transition region associated with the shadow boundary  $SB_1$  will be analyzed here; in this case  $SB_1$  exists within the domain  $0 < \phi < \pi$ . The analysis

for the transition region adjacent to  $SB_2$  in the domain  $-\pi < \phi < 0$  is similar.

The first integral in  $I_1$  can be solved by employing the usual integral representation for  $J_V(k\rho)$ , namely,

$$J_V(k\rho) = \frac{1}{2\pi} \int_{C_A+C_B} d\beta e^{-ik\rho \sin \beta + iv\beta} ,$$

and interchanging the orders of integration to yield

$$\begin{aligned} (11) \quad m \int_{C_1+C_2} J_{V(\tau)}(k\rho) e^{-iv(\tau)\psi} d\tau &= e^{-ik\rho \sin \psi} \\ &= e^{ik\rho \cos \phi} , \text{ for } 0 < \phi < \pi \text{ and } |\psi| < \frac{\pi}{2} . \end{aligned}$$

Clearly, (11) is just the incident field. In deriving (11) use is also made of the following.

$$\frac{\delta(\psi-\beta)}{m} = \frac{1}{2\pi} \int_{C_1+C_2} d\tau e^{-im(\psi-\beta)\tau} ,$$

where  $\delta(\psi-\beta)$  is the Dirac delta function.

Next, the second term on the R.H.S. of (10a) may be re-expressed in terms of the standard integral representation for  $H_{V(\tau)}^{(2)}(k\rho)$  as

$$\begin{aligned} & -\frac{m}{2} \int_{C_1} H_{V(\tau)}^{(2)}(k\rho) e^{-iv(\tau)\psi} d\tau \\ &= -\frac{m}{2} \int_{C_1} d\tau e^{-iv(\tau)\psi} \frac{1}{\pi} \int_{C_B} d\beta e^{-ik\rho \sin \beta + iv(\tau)\beta} \end{aligned}$$

which for  $\text{Im}(\tau) < 0$  reduces to

$$(12) \quad -\frac{\pi}{2} \int_{C_1} H_V^{(2)}(k\rho) e^{-iv(\tau)\psi} d\tau = \frac{e^{-ika\psi}}{2\pi i} \int_{C_B} d\beta \frac{e^{-ik\rho}}{\psi - \beta} [\sin \beta - \frac{a}{\rho} \beta];$$

with  $\psi = \phi - \frac{\pi}{2}$ ,  $|\psi| < \frac{\pi}{2}$  for  $0 < \phi < \pi$ .

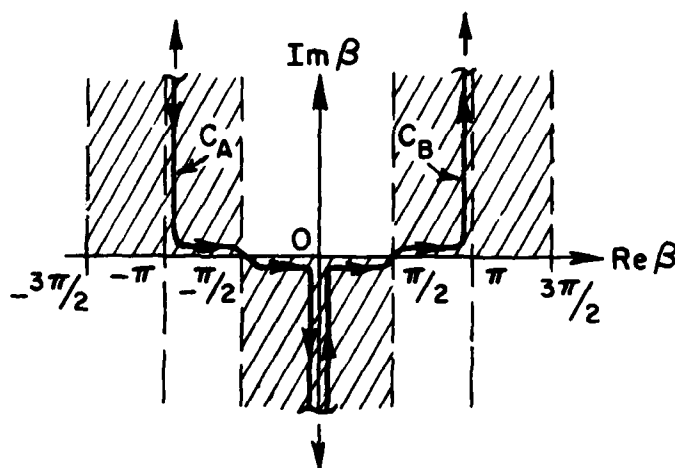


Fig. 4. Contours of integration for Bessel functions.

The contours of integration  $C_A$  and  $C_B$  occurring in the definitions of  $J_V(k\rho)$  and  $H_V^{(2)}(k\rho)$  are indicated in Fig. 4. The integrand on the R.H.S of (12) has a saddle point at  $\beta = \beta_s$ , where  $\beta_s = \cos^{-1} \frac{a}{\rho}$ . Since  $\beta_s$  is a constant for fixed values of  $\rho$  and  $a$ , it is conveniently determined by setting  $\phi = \phi_s$  (for which the observation point is on  $SB_1$ ); consequently,  $\beta_s = \frac{\pi}{2} - \delta_s = \phi_s - \frac{\pi}{2}$ , as shown in Fig. 2. Also, the integrand in (12) has a pole at  $\beta = \beta_p$ , where  $\beta_p = \psi = \phi - \frac{\pi}{2}$ . Let  $\theta \equiv \psi - \beta_s$ , then

$$(13) \quad \theta \equiv \psi - \beta_s = \beta_p - \beta_s = \phi - \phi_s.$$

When  $\phi > \phi_s$ , the field point is in the shadow region; therefore, it follows that  $\beta_p > \beta_s$  and  $\theta > 0$  in the shadow region. The integral on the R.H.S. of (12) can be evaluated via the method of steepest descent; hence, this integral over the contour  $C_B$  may be changed to an integral along the steepest descen path (SDP) through the saddle point  $\beta_s$  as indicated in Fig. 5. However, in the process of deforming the contour from  $C_B$  to SDP, the pole at  $\beta_p$  is crossed; it is therefore necessary to include it's residue in evaluating (12).

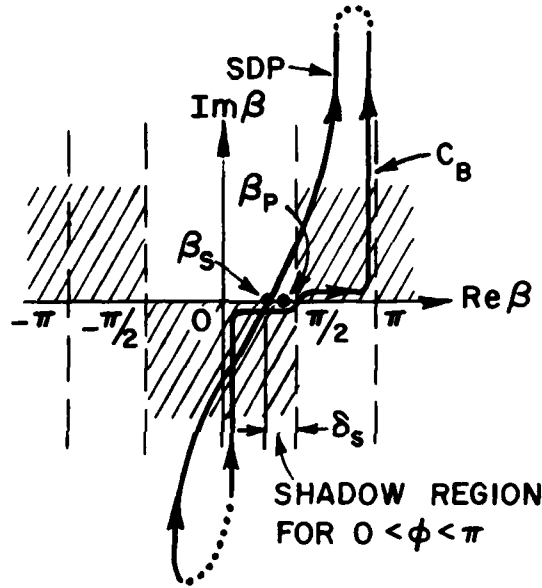


Fig. 5. Location of  $\beta_s$ ,  $\beta_p$  and SDP for the shadow region analysis.

The integral in (12) now becomes:

$$\begin{aligned}
 (14) \quad & \frac{e^{-ika\psi}}{2\pi i} \int_{C_B} d\beta \frac{e^{-ik\rho[\sin\beta - \frac{a}{\rho}\beta]}}{\beta - \psi} \\
 & = -e^{ik\rho \cos\phi} H(\phi - \phi_s) - \frac{e^{-ika\psi}}{2\pi i} \int_{SDP} d\beta \frac{e^{-ik\rho[\sin\beta - \frac{a}{\rho}\beta]}}{\beta - \psi}
 \end{aligned}$$

where the first term on the R.H.S. of (14) is the residue at  $\beta_p$ , and  $H(\phi - \phi_s)$  is the unit step function:

$$(15) \quad H(\phi - \phi_s) \equiv \begin{cases} 0 & , \phi < \phi_s \quad (\text{lit region}) \\ 1 & , \phi > \phi_s \quad (\text{shadow region}) \end{cases}$$

Therefore, the first term on the R.H.S. of (14) exactly cancels the incident field corresponding to (11) in the shadow. Approximating  $[\sin \beta - \frac{a}{\rho} \beta]$  in the exponent of the integrand on the R.H.S of (14) by its three term Taylor expansion about the saddle point  $\beta_s$  gives:

$$(16) \quad - \frac{e^{-ika\psi}}{2\pi i} \int_{SDP} d\beta \frac{e^{-ik\rho[\sin \beta - \frac{a}{\rho}\beta]}}{\beta - \psi} \\ \approx - \frac{e^{-iks - ika\theta}}{2\pi i} \int_{SDP} d\beta \frac{e^{iks[\frac{1}{2}(\beta - \beta_s)^2]}}{\beta - \beta_p},$$

where

$$(17) \quad s^2 \equiv \rho^2 - a^2.$$

The integral on the R.H.S of (16) is now in a form which can be readily evaluated asymptotically for large  $ks$  by the Pauli-Clemmow modified method of steepest descent [16,17] for a pole close to a saddle point, to yield the following result for the integral in (12).

$$(18) \quad - \frac{m}{2} \int_{C_1} H_v^{(2)}(k\rho) e^{-iv(\tau)\psi} d\tau \sim - e^{ik\rho \cos \phi} H(\phi - \phi_s) \\ + \frac{e^{-i\frac{\pi}{4}}}{\sqrt{2\pi k}} \frac{e^{-ika\theta}}{\theta} F[kL\tilde{a}] \frac{e^{-iks}}{\sqrt{s}},$$

where the function  $F[kL\tilde{a}]$  involves a Fresnel integral [17,18].



$$(19) \quad F[kL\tilde{a}] = 2i \sqrt{kL\tilde{a}} e^{ikL\tilde{a}} \int_{\sqrt{kL\tilde{a}}}^{\infty} e^{-i\tau^2} d\tau ;$$

in which one takes the positive branch of  $\sqrt{kL\tilde{a}}$ .

The distance parameter  $L$  in (19) for this case is

$$(20) \quad L = s ;$$

also, the quantity  $\tilde{a}$  in the argument  $kL\tilde{a}$  of  $F$  is

$$(21) \quad \tilde{a} = \frac{\theta^2}{2} .$$

It is noted that  $kL$  is always the large parameter in this asymptotic solution involving  $F[kL\tilde{a}]$ . Plots of the magnitude and phase of the function  $F[kL\tilde{a}]$  versus  $kL\tilde{a}$  are illustrated in Fig. 6. The physical significance of the geometric quantities  $\theta$  and  $s$  which appear in (18) is evident from Fig. 7. Combining (11) and (18), one obtains the following asymptotic result for  $I_1$ .

$$(22a) \quad I_1 \sim e^{ik\rho \cos \phi} + \left\{ - e^{ik\rho \cos \phi} H(\phi - \phi_s) + \frac{e^{-i\frac{\pi}{4}}}{\sqrt{2\pi k}} \frac{e^{-ika\theta}}{\theta} F[kL\tilde{a}] \frac{e^{-iks}}{\sqrt{s}} \right\} ; \quad \phi > \phi_s, \quad 0 < \phi < \pi .$$

Or,

$$(22b) \quad I_1 \sim \frac{e^{-i\frac{\pi}{4}}}{\sqrt{2\pi k}} \frac{e^{-ika\theta}}{\theta} F[kL\tilde{a}] \frac{e^{-iks}}{\sqrt{s}} ; \quad \phi > \phi_s, \quad 0 < \phi < \pi .$$

Turning next to the evaluation of  $I_2$  in (10b), it is observed that the integrals in (10b) can be simplified if the  $H_{\nu}^{(2)}(k\rho)$  terms appearing therein are replaced by the well known Debye approximation which is valid for  $\nu(\tau) < k\rho$  and  $\nu(\tau)$  large. Since  $\nu(\tau) = ka + m\tau$  and  $\nu(\tau) \sim 0(ka)$  in the transition region, the major contribution to the integrals in (10b) occur for  $\tau$  small. In this

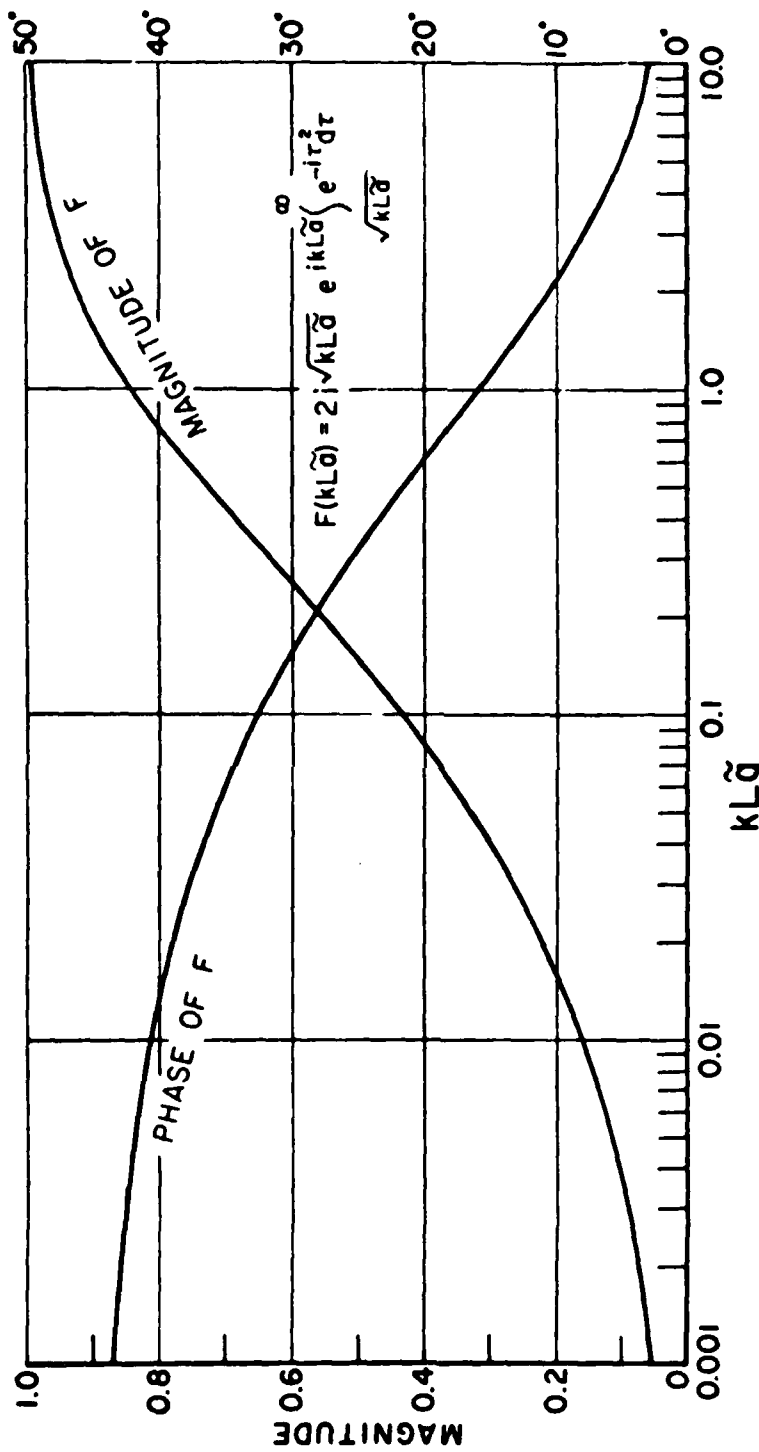
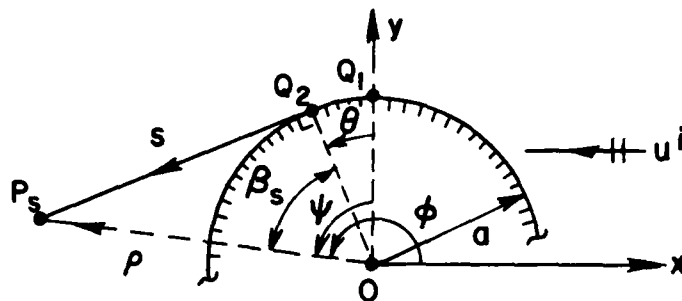


Fig. 6. Transition region correction factor  $F(kL\tilde{\alpha})$  (the positive branch of  $\sqrt{kL\tilde{\alpha}}$  is taken).



$$s^2 = \rho^2 - a^2$$

$$\beta_s = \cos^{-1} \frac{a}{\rho}$$

$$\theta = \psi - \beta_s > 0$$

Fig. 7. Geometrical parameters for the shadow region.

case,  $\frac{v(\tau)}{k\rho} = \frac{a}{\rho} + \tau \frac{m}{k\rho} \approx \frac{a}{\rho}$  so that  $v(\tau) < k\rho$  is satisfied, and the Debye approximation may be employed for  $H_{v(\tau)}^{(2)}(k\rho)$  as follows.

$$H_{v(\tau)}^{(2)}(k\rho) \sim \sqrt{\frac{2}{\pi k\rho \sin \gamma}} e^{-ik\rho \sin \gamma + iv(\tau)\gamma + i\frac{\pi}{4}};$$

with

$$v(\tau) < k\rho, \text{ and } \cos \gamma = \frac{v}{k\rho}.$$

When  $v(\tau) \sim 0(ka)$ ,  $\cos \gamma \approx \frac{a}{\rho}$  so that  $\gamma \approx \beta_s$ , and

$$\sin \gamma = \frac{[(k\rho)^2 - (v(\tau))^2]^{1/2}}{k\rho} \approx \frac{[k\rho^2 - a^2]^{1/2}}{k\rho} = \frac{s}{\rho}.$$

Incorporating these simplifications in the Debye approximation yields:

$$(23) \quad H_{v(\tau)}^{(2)}(k\rho) \sim \sqrt{\frac{2}{\pi ks}} e^{-iks + i\frac{\pi}{4}} e^{i(ka + m\tau)\beta_s}.$$

Next, incorporating (23), and the relation  $\tilde{Q} W_1(\tau) = \tilde{Q} W_2(\tau) + 2 i \tilde{Q} V(\tau)$  into the integrals in (10b) leads to the following expression for  $I_2$ :

$$(24a) \quad I_2 \sim \sqrt{\frac{2}{ks}} e^{-iks} - ika\theta m \frac{e^{i\frac{\pi}{4}}}{\sqrt{\pi}} \left[ \frac{1}{2} \int_{C_1} e^{-im\tau\theta} d\tau + i \int_{C_1+C_2} \frac{\tilde{Q} V(\tau)}{\tilde{Q} W_2(\tau)} e^{-im\tau\theta} d\tau \right].$$

$I_2$  can be further simplified in a straight forward manner to obtain:

$$(24b) \quad I_2 \sim - \frac{e^{-i\frac{\pi}{4}}}{\sqrt{2\pi k}} e^{-ika\theta} \frac{e^{-iks}}{\theta} - m \sqrt{\frac{2}{k}} e^{-ika\theta} \hat{p}_{s,h}(\xi) \frac{e^{-iks}}{\sqrt{s}}$$

where  $\hat{p}_{s,h}(\xi)$  is the Pekeris caret function [9] defined by:

$$(25) \quad \hat{p}_{s,h}(\xi) \equiv \frac{e^{-i\frac{\pi}{4}}}{\sqrt{\pi}} \int_{-\infty}^{\infty} \frac{\tilde{Q} V(\tau)}{\tilde{Q} W_2(\tau)} e^{-i\xi\tau} d\tau,$$

and the parameter  $\xi$  is defined by

$$(26) \quad \xi \equiv m\theta \quad (\xi > 0 \text{ in the shadow region}).$$

The subscript  $s$  on  $\hat{p}_s$  is used to denote the  $TM_z$  (or acoustical soft) case; whereas, the subscript  $h$  on  $\hat{p}_h$  denotes the  $TE_z$  (or acoustical hard) case. Values of  $\hat{p}_{s,h}(\xi)$  versus  $\xi$  are presented in Fig. 8 in terms of related functions  $p^*(\xi)$  and  $q^*(\xi)$ .

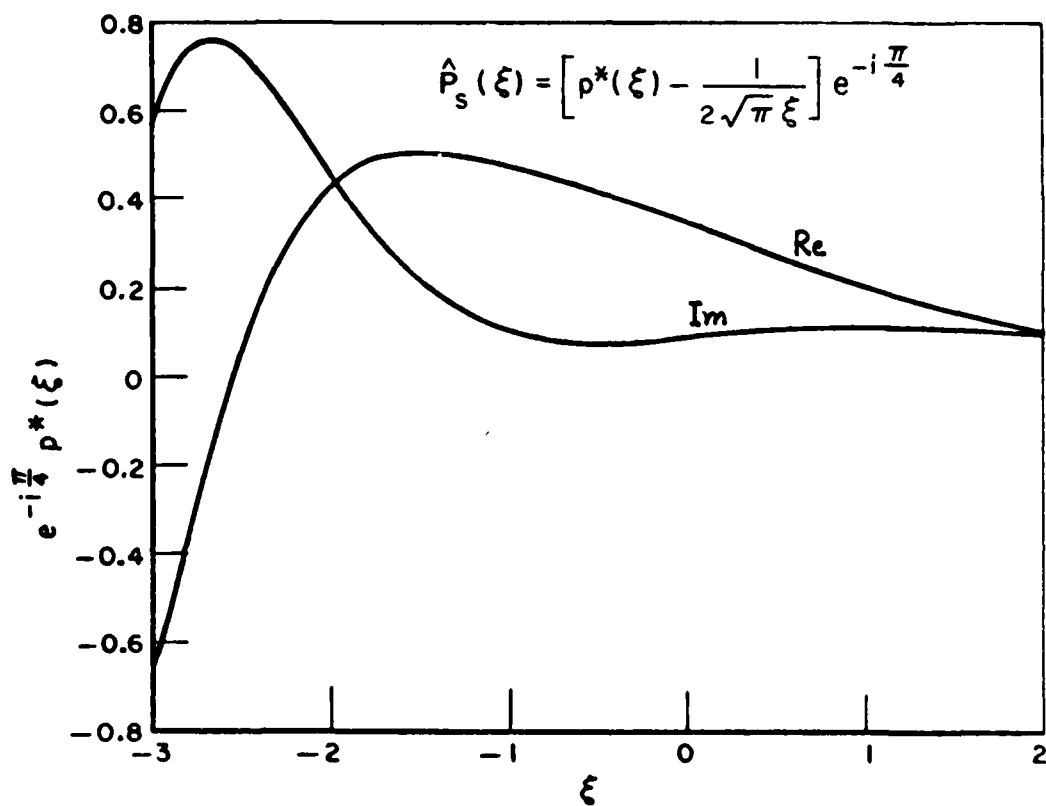


Fig. 8(a). Plot of  $e^{-i\pi/4} p^*(\xi)$  versus  $\xi$  based on Logan's tabulated data [9] for  $p(\xi)$ .

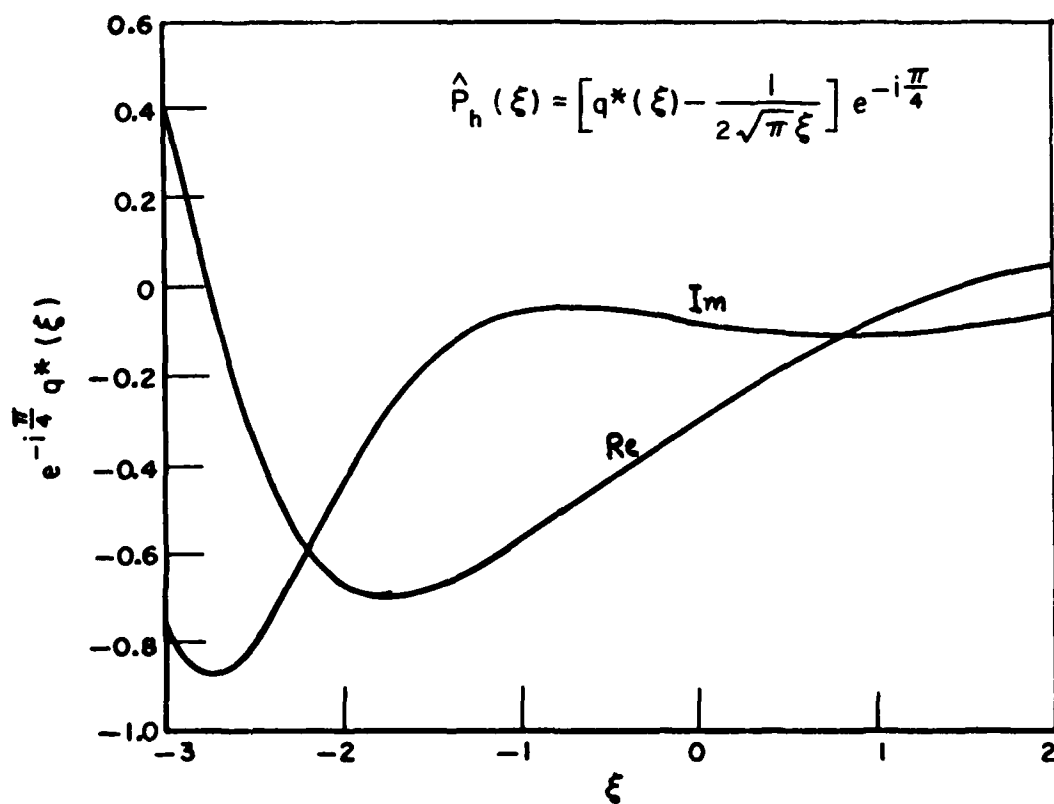


Fig. 8(b). Plot of  $e^{-i\pi/4} q^*(\xi)$  versus  $\xi$  based on Logan's tabulated data [9] for  $q(\xi)$ .

Combining the results of (22b) and (24b), one obtains the following asymptotic expression for  $U$  (of Eq. (9)) which is valid at the observation point  $P_S$  in the shadowed portion of the transition region.

$$(27) \quad U(P_S) \sim - \frac{e^{-i\frac{\pi}{4}}}{\sqrt{2\pi k}} \frac{e^{-ika\theta}}{\theta} \left\{ 1 - F[kL\tilde{a}] \right\} \frac{e^{-iks}}{\sqrt{s}} \\ - m \sqrt{\frac{2}{k}} e^{-ika\theta} \hat{p}_S(\xi) \frac{e^{-iks}}{\sqrt{s}} \quad ; \quad \theta > 0, \phi > \phi_S, \xi > 0.$$

The above result for  $U$  may be interpreted geometrically as a field which after being launched by the incident wave at  $Q_1$  propagates along the path  $Q_1Q_2P_S$  to the field point  $P_S$ , as indicated in Fig. 7.  $Q_1$  and  $Q_2$  are tangent points which correspond to the point of grazing incidence on the cylinder, and the point of tangential shedding of the diffracted wave from the surface, respectively.

One may now examine the result of directly extending the analysis presented above to lit region. In the lit region,  $\phi < \phi_S$  and  $\beta_p < \beta_S$  as indicated in Fig. 9 (note: Fig. 5 shows  $\beta_p > \beta_S$  in shadow region). Consequently,  $H(\phi - \phi_S) = 0$ ; also,  $\theta < 0$  ( $\xi < 0$ ) for  $\phi < \phi_S$ , and the field  $U$  at the point  $P_L$  in the lit region becomes via (22a) and (24b):

$$(28) \quad U(P_L) \sim e^{ik\rho \cos\phi} - \frac{e^{-i\frac{\pi}{4}}}{\sqrt{2\pi k}} \frac{e^{-ika\theta}}{\theta} \left\{ 1 - F[kL\tilde{a}] \right\} \frac{e^{-iks}}{\sqrt{s}} \\ - m \sqrt{\frac{2}{k}} e^{-ika\theta} \hat{p}_S(\xi) \frac{e^{-iks}}{\sqrt{s}} \quad ; \quad \phi < \phi_S; \theta < 0; \xi < 0.$$

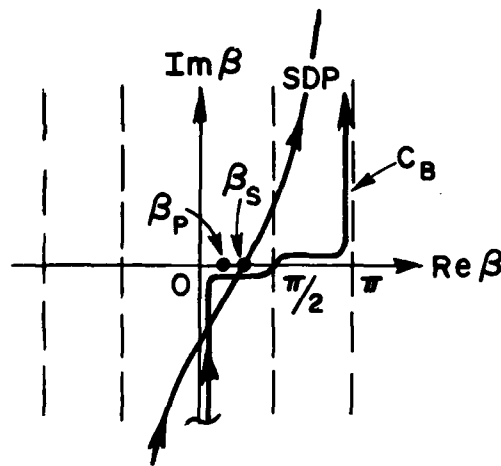


Fig. 9. Location of  $\beta_S$ ,  $\beta_P$  and SDP for the lit region.

Equations (27) and (28) may be represented compactly in a single expression as follows:

$$(29) \quad U(P) \sim e^{ik\rho \cos\phi} H(-\theta) - \frac{e^{-i\frac{\pi}{4}}}{\sqrt{2\pi k}} \frac{e^{-ika\theta}}{\theta} \left\{ 1 - F \left[ \frac{kL\xi^2}{2m^2} \right] \right\} \frac{e^{-iks}}{\sqrt{s}} \\ - m \sqrt{\frac{2}{k}} e^{-ika\theta} \hat{p}_{S_h}(\xi) \frac{e^{-iks}}{\sqrt{s}}$$

with:  $kL\tilde{a} = kL\frac{\xi^2}{m^2}$ ,  $\xi = m\theta$ ,  $L = s$ ; also,

$P = P_L$ , for  $\xi < 0$ ,  $\theta < 0$ , and  $\phi < \phi_S$  (in the lit region),

$P = P_S$ , for  $\xi > 0$ ,  $\theta > 0$ , and  $\phi > \phi_S$  (in the shadow region),

$$H(-\theta) = \begin{cases} 1, & \theta < 0 \text{ for } P = P_L \\ 0, & \theta > 0 \text{ for } P = P_S \end{cases}.$$



$$\theta = \psi - \beta_s < 0$$

The result in (29) will be shown to be finite and continuous across  $SB_1$ . As one approaches  $SB_1$ ,  $\phi \rightarrow \phi_S$  and  $\theta \rightarrow 0$ ; hence,  $\tilde{a} = \frac{\theta^2}{2} \rightarrow 0$  and  $\xi \rightarrow 0$ . The limiting forms of  $F[kL\tilde{a}]$  and  $\hat{P}_S(\xi)$  as  $\theta, \xi \rightarrow 0$  are [18,19]:

$$(30a) \quad F[kL\tilde{a}] \approx \left( \left| \sqrt{\pi kL\tilde{a}} \right| - 2 kL\tilde{a} e^{i\frac{\pi}{4}} \right) e^{i\left(\frac{\pi}{4} + kL\tilde{a}\right)},$$

for a given  $kL$  as  $\tilde{\alpha} \rightarrow 0$ ; and

$$(30b) \quad \hat{P}_{S,h}(\xi) \equiv \left[ \frac{p^*(\xi)}{q^*(\xi)} - \frac{1}{2\sqrt{\pi\xi}} \right] e^{-i\frac{\pi}{4}} + \frac{e^{-i\frac{\pi}{4}}}{2\sqrt{\pi\xi}} + (\text{small contribution from } p^* \text{ or } q^* \text{ which is continuous w.r.t. } \xi), \text{ as } \xi \rightarrow 0.$$

(Note: the  $p^*(\xi)e^{-i\frac{\pi}{4}}$  and  $q^*(\xi)e^{-i\frac{\pi}{4}}$  functions are plotted in Fig. 8.)

Employing the above limiting forms of (30a; 30b) in (29) as  $\theta, \xi \rightarrow 0$  from both, the lit ( $\theta, \xi < 0$ ) and shadow ( $\theta, \xi > 0$ ) directions, it is easily verified that  $U$  in (29) is finite and continuous across  $SB_1$ ; in fact, exactly at  $SB_1$ ,  $U(P)$  becomes:

$$(31) \quad U(P) \Big|_{SB_1} \sim \frac{1}{2} e^{ikx} - m \sqrt{\frac{2}{k}} e^{-i\frac{\pi}{4}} \left\{ \frac{p^*(0)}{q^*(0)} \right\} \frac{e^{ikx}}{|\sqrt{x}|};$$

for  $\begin{cases} TM_z \text{ case} \\ TE_z \text{ case} \end{cases}$ ,

where  $x = \rho \cos \phi_s = -s$  along  $SB_1$  (a similar result holds for  $SB_2$ ).

The first term on the R.H.S. of (31) is simply one-half the incident field on the shadow boundary as in the diffraction by a half-plane; the second term is dependent on surface properties.

Turning now to the evaluation of the field in the shadow region, but away from  $SB_1$  and exterior to the transition region (i.e., in region III of Fig. 1), one notes that  $F[kL\tilde{\alpha}] \rightarrow 1$  since  $\theta$ , and hence  $kL\tilde{\alpha}$  become large in this case (see Fig. 6); only the term containing  $\hat{P}_{S,h}(\xi)$  in (29) now remains significant. Far from  $SB_1$  the integral

for  $\hat{P}_{S,h}(\xi)$  in (25) may be replaced by a rapidly convergent residue series [9]:

$$(32) \quad \hat{P}_{S_h}(\xi) \Big|_{\xi > 0} = \begin{cases} -\frac{e^{-i\frac{\pi}{4}}}{\sqrt{\pi}} \sum_n \frac{e^{\frac{i\pi}{6}} e^{\xi q_n} e^{-i\frac{5\pi}{6}}}{2[Ai'(-q_n)]^2}, & \text{for } \tilde{Q}=1 \text{ or TM}_z \text{ case} \\ -\frac{e^{-i\frac{\pi}{4}}}{\sqrt{\pi}} \sum_n \frac{e^{\frac{i\pi}{6}} e^{\xi \bar{q}_n} e^{-i\frac{5\pi}{6}}}{2[Ai'(-\bar{q}_n)]^2 \bar{q}_n}, & \text{for } \tilde{Q} = \frac{\partial}{\partial \tau} \text{ or TE}_z \text{ case} \end{cases}$$

where  $Ai$  is the Miller-type Airy function\* (which is related to the Fock-type Airy function [9]), and  $Ai'$  is its derivative with respect to the argument. The  $q_n$  and  $\bar{q}_n$  are roots of  $Ai(-q_n) = 0$  and  $Ai'(-\bar{q}_n) = 0$ , respectively for  $n = 1, 2, 3, \dots$ . These roots are tabulated in [9].

When the above residue series representation of (32) is employed in  $\hat{P}_{S_h}(\xi)$  of (29) for  $kLa \gg 10$  (i.e., as  $F[kLa] \rightarrow 1$ ), it

can be readily shown that (29) reduces to

$$(33) \quad U(P_S) \sim U^i(Q_1) \left[ \sum_n \frac{S}{D_n^h(Q_1)} e^{-ika\theta} - \alpha_n^h a\theta \frac{S}{D_n^h(Q_2)} \right] \frac{e^{-iks}}{\sqrt{s}},$$

where  $D_n^h$  and  $\alpha_n^h$  are the Keller diffraction and attenuation coefficients [3] associated with the GTD surface ray modes, respec-

tively, with  $D_n^h(Q_1) = D_n^h(Q_2)$  for the circular cylinder. The

superscripts in  $D_n^h$  and  $\alpha_n^h$  correspond exactly to the subscripts in  $\hat{P}_{S_h}(\xi)$  for the two polarizations; also, the subscript  $n$  denotes the

---

\*  $Ai(\tau) = V(\tau)/\sqrt{\pi} = \frac{1}{2\pi} \int_{-\infty}^{\infty} dt e^{-i(\tau t + t^3/3)}$ ;  $Ai'(\tau) = \frac{dAi(\tau)}{d\tau}$ .

surface ray modal index. The  $U^i(q_1)$  in (33) represents the incident field at  $q_1$  and is unity for this problem. Thus, in the deep shadow (i.e., corresponding to region III of Fig. 1), (29) reduces to the GTD surface diffracted ray field given by (33) as it should. The geometrical interpretation of the GTD field in (33) is, of course, identical to that in Fig. 7. For the sake of convenience, and completeness, the diffraction and attenuation coefficients in (33) are listed below.

$$[D_n^s]^2 \sim \frac{\sqrt{\pi} 2^{-5/6} \rho_g^{1/3} e^{-i\pi/12}}{K^{1/6} [Ai'(-q_n)]^2}; \alpha_n^s \sim \frac{q_n}{\rho_g} e^{i\pi/6} \left(\frac{k\rho_g}{2}\right)^{1/3}$$

$$[D_n^h]^2 \sim \frac{\sqrt{\pi} 2^{-5/6} \rho_g^{1/3} e^{-i\pi/12}}{K^{1/6} \bar{q}_n [Ai(-\bar{q}_n)]^2}; \alpha_n^h \sim \frac{\bar{q}_n}{\rho_g} e^{i\pi/6} \left(\frac{k\rho_g}{2}\right)^{1/3}$$

#### B. Transition Region - Illuminated Zone

Although the result in (29) is applicable to both the shadow and lit portions of the transition region, it does not reduce to the geometrical optics field in the lit region. Consequently, the result in (29) is expected to be accurate in the shadow region both near and far from  $SB_1$ ; whereas, it is expected to be accurate only for  $\theta$  small in the lit region ( $\xi, \theta < 0$ ). This deficiency of (29) for the lit region where  $\theta$  is not small is briefly discussed, and an improved solution which overcomes this difficulty is presented.

For the shadowed part of the transition region, the result in (29) has the geometrical interpretation illustrated in Fig. 7 which is identical to the GTD surface diffracted ray picture as shown in Fig. 1; consequently, it is not too surprising that Eq. (29) does indeed reduce exactly to the GTD solution of Eq. (33) in the deep shadow. On the other hand, the geometrical interpretation of the scattered field in (29) for the lit region ( $\theta < 0$ ) is illustrated in Fig. 10 which constitutes a direct generalization of the interpretation in Fig. 7 (for  $\theta > 0$ ); clearly, the ray geometry in Fig. 10 is in disagreement with the geometrical optics reflected ray picture of Fig. 11 which is known to be valid in the lit region. Consequently, one might anticipate the failure of Eq. (29) to reduce to the geometrical optics field in the lit region as a result of the differences between the scattered field propagation mechanisms of Figs. 10 and 11.

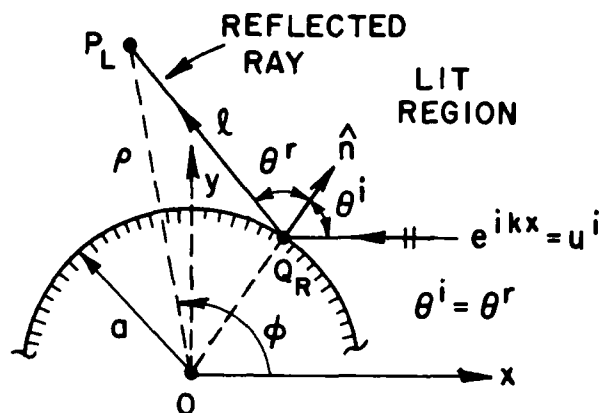


Fig. 11. Reflected ray system.

From Fig. 10, it is observed that the scattered field at  $P_L$  traverses the path  $Q_1 Q_3 P_L$  after being launched by the incident wave at  $Q_1$ . This interpretation requires the field to propagate backward from  $Q_1$  to  $Q_3$  and then shed to  $P_L$  along the backward tangent at  $Q_3$ ; in contrast, the geometric optical reflected ray trajectory touches the surface only at  $Q_R$  as in Fig. 11. The paths in Figs. 7 and 11 satisfy the extended Fermat's principle; whereas, the ray path in Fig. 10 does not. The inability of Eq. (29) to reduce to the geometrical optics field may be explained on the basis of the approximation in (23) for the Hankel function  $H_{\nu}^{(2)}(k\rho)$  which is employed in the evaluation of the transition region field; more will be said about this shortly.

For the sake of completeness, the behavior of Eq. (29) in the deep lit region is examined. As before,  $F[kL\hat{\alpha}] \rightarrow 1$  as the field point moves away from  $SB_1$  in both the lit and shadow zones, thereby leaving the term containing  $P_s(\xi)$  as the dominant con-

tributor to the scattered field. Hence, in the lit region far from  $SB_1$  where  $\xi \ll 0$ , Eq. (29) reduces to

$$(34) \quad U(P_L) \sim e^{ik\rho \cos \phi} H(-\theta) - m \sqrt{\frac{2}{k}} e^{-ika\theta} \hat{p}_{S_h}(\xi) \frac{e^{-iks}}{\sqrt{s}},$$

$$\theta < 0, \xi < 0.$$

When  $\xi \ll 0$ ,  $\hat{p}_{S_h}(\xi)$  has the following asymptotic value [9]

$$(35) \quad \hat{p}_{S_h}(\xi) \sim \pm \frac{\sqrt{-\xi}}{2} e^{i\frac{\xi^3}{12}} [1 + O(\xi^{-3})] ; \quad \xi < 0.$$

Incorporating (35) into (34), one arrives at the following

$$(36) \quad U(P_L) \sim U^i(P_L) \mp \sqrt{\frac{a|\theta|}{4}} e^{ika[|\theta| - \frac{|\theta|^3}{24}]} \frac{e^{-iks}}{\sqrt{s}}$$

$$\text{for } \begin{cases} TM_z \\ TE_z \end{cases} \text{ case when } \xi < 0.$$

On the other hand, the geometrical optics field represents the correct asymptotic result far from  $SB_1$  in the lit region, and its field associated with the incident and reflected rays is well known to be

$$(37) \quad U(P_L) \sim U^i(P_L) \mp U^i(Q_R) \sqrt{\frac{\rho_r}{\rho_r + \ell}} e^{-ik\ell}$$

where  $U^i(P_L) = e^{ik\rho \cos \phi}$  and  $U^i(Q_R) = e^{ika \cos \theta^i}$  (see Fig. 11). The first term on the RHS of Eq. (37) is the incident field at  $P_L$ , and the second term denotes the reflected ray field.  $Q_R$  is the point of reflection on the surface as shown in Fig. 11, and the  $\{\mp\}$  sign in front of  $U^i(Q_R)$  denotes the value of the surface reflection coefficient at  $Q_R$  for the  $\begin{cases} TE_z \\ TM_z \end{cases}$  case. The spatial distance  $\ell$  is given by  $\ell = Q_R P_L$ ; whereas, the caustic distance  $\rho_r$  associated with the reflected field is

$$(38) \quad \rho_r = \frac{a \cos \theta^i}{2}.$$

The quantities  $\rho$  and  $\theta^i$  are also shown in Fig. 11.

One notes that Eq. (36) and Eq. (37) are nearly equal only for  $\theta$  very small. In general, therefore, the result of Eq. (29) fails to reduce the geometrical optics result when  $\xi \ll 0$  (this failure is similar to that which occurs in the results of [7], [8], and [14]); consequently, in order to overcome this limitation, one must employ an approximation for  $H_{v(\tau)}^{(2)}(k\rho)$  in the lit region which is different from that in (23), and which leads to a geometrical interpretation for the scattered field in the lit region which is in agreement with the reflected ray geometry of Fig. 11.

The approximation of  $H_{v(\tau)}^{(2)}(k\rho)$  in (23) is valid for  $v(\tau) \sim 0(ka)$ ; the condition  $v(\tau) \sim 0(ka)$  holds in the transition region near  $SB_1$  and also in the deep shadow zone where only the first couple of GTD surface ray modes (corresponding to  $n = 1, 2$ , etc., in (32) and (33)) are necessary to describe the field accurately; whereas, deep in the lit region  $v(\tau)$  can be significantly different from  $ka$ . Thus, Eq. (23) leads to the result of Eq. (29) which is accurate in the shadow region, but it is not expected to be accurate in the lit region if the field point is not close to  $SB_1$ .

The Fock-type Airy terms  $\tilde{Q} V(\tau)$ , and  $\tilde{Q} W_1(\tau)$  in (10b) which approximate  $J_v(ka)$  and  $H_v^{(2)}(ka)$  for  $v \sim 0(ka)$  reduce uniformly to the Debye asymptotic approximations when  $\tau$  becomes large ( $\tau = \frac{v - ka}{m}$ ); hence, in contrast to the approximation for  $H_{v(\tau)}^{(2)}(k\rho)$  in (23), these Fock-type Airy functions remain valid as  $v(\tau)$  becomes different from  $ka$  (i.e., for  $|v - ka| > 0(m)$ ) deep in the lit region. Instead of the approximation in (23), one could also approximate  $H_{v(\tau)}^{(2)}(k\rho)$  for the near zone case by the Fock-type Airy function  $W_2$  as follows, provided  $k[\rho - a] \ll ka$ .

$$(39) \quad H_{v(\tau)}^{(2)}(k\rho) \approx \frac{i}{m\sqrt{\pi}} W_2(\tau - m^{-1}k[\rho - a]) \quad ; \quad k[\rho - a] \ll ka.$$

But, employing the near zone approximation of Eq. (39) in  $I_2$  of Eq. (10b) leads to integrals which are complicated functions of two parameters (namely,  $\psi$  and  $[\rho - a]$ ); on the other hand, the result in (29) is in terms of simpler  $F$  and  $P_h$  integrals which are

each functions of only a single parameter.

A representation for  $U$  in the lit region which is interpretable in terms of the desired reflected ray geometry of Fig. 11 and which also is in terms of the  $F$  and  $\hat{P}_S$  functions may be obtained in the following

manner by incorporating an approximation for  $H_{v(\tau)}^{(2)}(k\rho)$  which unlike (23) is valid even if  $v$  becomes quite different from  $ka$  in the lit region. One begins by introducing the Debye approximation for  $H_{v(\tau)}^{(2)}(k\rho)$  which was previously indicated as

$$(40) \quad H_{v(\tau)}^{(2)}(k\rho) \sim \sqrt{\frac{2}{\pi k\rho \sin \gamma}} e^{-ik\rho \sin \gamma + iv(\tau)\gamma + i\frac{\pi}{4}};$$

$$v(\tau) = k\rho \cos \gamma \text{ and } v(\tau) < k\rho.$$

The condition that  $v(\tau) < k\rho$  be satisfied in the lit zone is verified in the Appendix where the geometric optical reflected field result (corresponding to the second term on the R.H.S. of Eq. (37)) is developed in detail. Referring to this development in the Appendix, it is seen that in the lit region where  $v < ka$ , the following approximations are valid:

$$(41a) \quad v(\tau) \approx v_0 = ka \cos \tilde{\gamma}_0 = k\rho \cos \gamma_0 \quad ; \quad \gamma \approx \gamma_0$$

$$(41b) \quad \sin \tilde{\gamma}_0 = \cos \theta^i, \text{ since } \tilde{\gamma}_0 = \frac{\pi}{2} - \theta^i$$

$$(41c) \quad \rho \sin \gamma \approx \rho \sin \gamma_0 = \ell + a \sin \tilde{\gamma}_0 = \ell + a \cos \theta^i$$

$$(41d) \quad \psi \approx \gamma_0 - 2 \tilde{\gamma}_0$$

(Note: the geometrical significances of (41) is shown in Fig. A-I in the Appendix.)

The quantity  $\psi$  has already be defined, and  $\tilde{\gamma}_0$  is introduced in the Appendix. The subscript  $o$  in  $v_0(\tau)$ ,  $\gamma_0$  and  $\tilde{\gamma}_0$  refers to the geometrical optics reflected field saddle point condition which is also discussed in the Appendix. Incorporating  $v(\tau)\gamma \approx v(\tau)\gamma_0$ ;  $\rho \sin \gamma \approx \ell + a \cos \theta^i$  for the phase; and  $\rho \sin \gamma \approx \ell$  for



the far zone amplitude via (41a) and (41c) leads to the following far-zone approximation (in contrast to the near-zone approximation of Eq. (39)) for  $H_{V(\tau)}^{(2)}(k\rho)$  in the lit zone.

$$(42) \quad H_{V(\tau)}^{(2)}(k\rho) \sim \sqrt{\frac{2}{\pi k \ell}} e^{-ik(\ell + a \cos \theta^i) + i v(\tau) \gamma_0 + i \frac{\pi}{4}}.$$

Next, incorporating (41d), (42), and  $\tilde{Q} W_1(\tau) = \tilde{Q} W_2(\tau) + 2 i \tilde{Q} V(\tau)$  into (10b) yields:

$$(43) \quad I_2 \sim - \sqrt{\frac{2}{k \ell}} e^{-ik \ell} e^{-ika \cos \theta^i} m e^{-ika(-2 \tilde{\gamma}_0)} \cdot \left[ \frac{e^{-i \frac{\pi}{4}}}{2 \sqrt{\pi} [m(-2 \tilde{\gamma}_0)]} + \frac{e^{-i \frac{\pi}{4}}}{\sqrt{\pi}} \int_{-\infty}^{\infty} \frac{\tilde{Q} V(\tau)}{\tilde{Q} W_2(\tau)} e^{-im(-2 \tilde{\gamma}_0)\tau} d\tau \right].$$

One now defines  $\xi'$  for the lit region as

$$(44) \quad \xi' \equiv -2 m \sin \tilde{\gamma}_0 = -2 m \cos \theta^i ; \quad \xi' < 0 \text{ in the lit region.}$$

Thus, the exponential terms involving  $\tilde{\gamma}_0$  in (43) may be written as

$$(45a) \quad e^{-ika(-2 \tilde{\gamma}_0)} \sim e^{2 ika \cos \theta^i - i(\xi')^3/12}$$

and

$$(45b) \quad e^{-im(-2 \tilde{\gamma}_0)\tau} \sim e^{-i\xi'\tau}$$

provided that  $\xi'$  is sufficiently small in comparison with  $m$  which is assumed large so that terms  $O\left(\frac{1}{[2m]^2}\right)$  and higher may be neglected

in the exponent. This approximation is valid in the transition region. One notes that the approximation in (45a) and (45b) follow directly from the expansion

$$(45c) \quad -\tilde{\gamma}_0 = \sin^{-1} \frac{\xi'}{2m} = \frac{1}{2m} \xi' + \frac{1}{6(2m)^3} (\xi')^3 + \frac{3}{40(2m)^5} (\xi')^5 + \dots,$$

$$\text{with } \left( \frac{\xi'}{2m} \right)^2 < 1.$$

Employing (45a) and (45b) into (43) yields

$$(46) \quad I_2 \sim \sqrt{\frac{2}{k\ell}} e^{-ik\ell} e^{-ika \cos \theta^i} e^{i2ka \cos \theta^i} \cdot e^{-i(\xi')^3/12} \left[ \frac{e^{-i\frac{\pi}{4}}}{2\sqrt{\pi\xi'}} + \hat{p}_s(\xi') \right],$$

which is valid in the far zone. In the lit region far from SB<sub>1</sub>,  $\xi' < 0$ , and  $\hat{p}_s(\xi)$  may be replaced by (35) to yield

$$(47) \quad I_2 \sim \mp e^{ika \cos \theta^i} \sqrt{\frac{\rho_r}{\ell}} e^{-ik\ell},$$

which does indeed agree with the far zone geometrical optics reflected field. The term  $e^{ika \cos \theta^i}$  corresponds exactly to  $U^1(Q_r)$ , and  $\{\mp\}$  denotes the reflection coefficient values as in (37).

It is now evident that one can employ ray optics to generalize (46) so that it yields the near zone geometrical optics reflected field as in (37). According to ray optics, the far zone energy spread

factor  $\sqrt{\frac{\rho_r}{\ell}}$  in (47) must be simply replaced by its corresponding near zone factor  $\sqrt{\frac{\rho_r}{\rho_r + \ell}}$  (as in (37)) for the reflected ray tube in order to extend (47) to the near zone case; the latter is tantamount to replacing  $\frac{1}{\sqrt{\ell}}$  in (46) with  $\frac{1}{\sqrt{\rho_r + \ell}}$  thereby generalizing (46) to the near zone case.

To be consistent, it is also necessary to modify the result for  $I_1$  of (10a) for the lit region in the same manner as done above for  $I_2$  of (10b). Without giving all the details (since these involve essentially the same physical arguments as in the treatment of  $I_2$ ), the result for  $I_1$  in the lit region becomes

$$(48a) \quad I_1 \sim e^{ik\rho \cos\phi} H(-\theta) - e^{ika \cos\theta} \cdot \left\{ \frac{m e^{-i\frac{\pi}{4}}}{\sqrt{2} \pi k \xi'} \left( -F\left[kL' \frac{\xi'^2}{2m^2}\right] \right) \right\} e^{-\frac{i(\xi')^3}{12}} \frac{e^{-ik\ell}}{\sqrt{\ell + \rho_r}},$$

with

$$(48b) \quad L' \equiv \ell, \text{ for } \xi' < 0.$$

Finally, combining (46) (together with its near zone modification) and (48), one obtains the required result for  $U$  in the lit region; namely,

$$(49) \quad U(P_L) \sim U^i(P_L) + U^i(Q_R) \left[ \frac{-m e^{-i\frac{\pi}{4}}}{\sqrt{2} \pi k \xi'} e^{-\frac{i(\xi')^3}{12}} \cdot \left\{ 1 - F\left[kL' \frac{\xi'^2}{2m^2}\right] \right\} \frac{e^{-ik\ell}}{\sqrt{\ell + \rho_r}} \right. \\ \left. + U^i(Q_R) \left[ -m \sqrt{\frac{2}{k}} e^{-\frac{i(\xi')^3}{12}} \hat{p}_s(\xi') \right] \frac{e^{-ik\ell}}{\sqrt{\ell + \rho_r}} \right]; \quad \xi' < 0.$$

It is easily verified that far from  $SB_1$  ( $\xi' \ll 0$ ),  $F\left[kL' \frac{\xi'^2}{2m^2}\right] \rightarrow i$

and  $\hat{p}_s(\xi')$  behaves as in (35) so that in the deep lit regions Eq. (49) reduces exactly to the geometrical optics result of Eq. (37).

Furthermore, Eq. (49) is also valid for  $\theta \rightarrow \pi/2$  (i.e., near  $SB_1$ ) since it agrees in this limiting case with the expression in (29) for  $\xi < 0$ . In addition, Eq. (49) reduces to Eq. (31), thereby assuring the boundedness and continuity of the field across  $SB_1$ . Thus, the result for  $U$  in (49) for the lit region reduces to the geometrical optics field deep in the illuminated region where the latter is indeed valid, and at the same time it has the proper behavior required to ensure the continuity of the field across  $SB_1$ .

### III. NUMERICAL RESULTS

In this section, numerical results are presented for the near zone total field surrounding a perfectly-conducting circular cylinder excited by a plane wave. The GTD method is employed to describe the field exterior to the cylinder in terms of the geometrical optics incident and reflected rays for the lit region, and in terms of the surface diffracted rays for the shadow region, respectively; these results for the  $TE_z$  (hard boundary) case are indicated in Figs. 12(a) - 20(a) for different size cylinders and near field distances. It is seen that the GTD solution shown by a dashed line becomes discontinuous at the shadow boundaries. On the other hand, the present transition region solution (based on (27) for the shadow, and on (49) for the lit region) as indicated by a solid line is continuous across the shadow boundaries, and it blends smoothly into the GTD solution outside the transition region. These GTD and transition region solutions corresponding to Figs. 12(a) - 20(a) are combined into a single, composite GTD-transition solution which is shown by a smooth solid curve in Figs. 12(b) - 20(b), respectively. The composite GTD-transition results are compared against results which are based on an exact eigenfunction series solution for these cases; the eigenfunction results are shown by dots in Figs. 12(b) - 20(b) for these cases. Figures 12(b) - 20(b) indicate that the comparison between the numerical results obtained from the exact eigenfunction solution, and the composite GTD-transition solution is very good, thereby confirming the accuracy of the uniform result for the transition region presented in section II. Additional comparisons of the composite GTD-transition solutions with the corresponding eigenfunction solutions are indicated in Figs. 21-22 for the  $TM_z$  (soft boundary) case, respectively; again the agreement is very good for these cases. It is seen that the accuracy of the transition region solution for very small  $ka$  and  $k\rho$  is as good as the accuracy of the geometrical optics result.\* As  $ka$  and  $k\rho$  increase, our asymptotic transition field solution becomes increasingly accurate as do the GTD (surface diffracted and geometric optical) ray fields which also are asymptotic approximations. For calculating the GTD field in the shadow region, the inclusion of only two surface ray modes are found to be sufficiently accurate (see (33)). Unfortunately, there appears to be a small error in the  $p^*$  function plotted in Fig. 8(a); this error is noticeable for ranges of  $\xi$  which occur for small  $k\rho$  and  $ka$  in the  $TM_z$  case. Presently, improved curves for the amplitude and phase of  $p^*(\xi)$  are being obtained.

---

\*In the GTD calculation for the lit region (or the geometrical optics region), the surface rays that have crept around the opposite side of the cylinder have been neglected; but the field of these rays is included with the transition field in the calculation shown by the solid line.

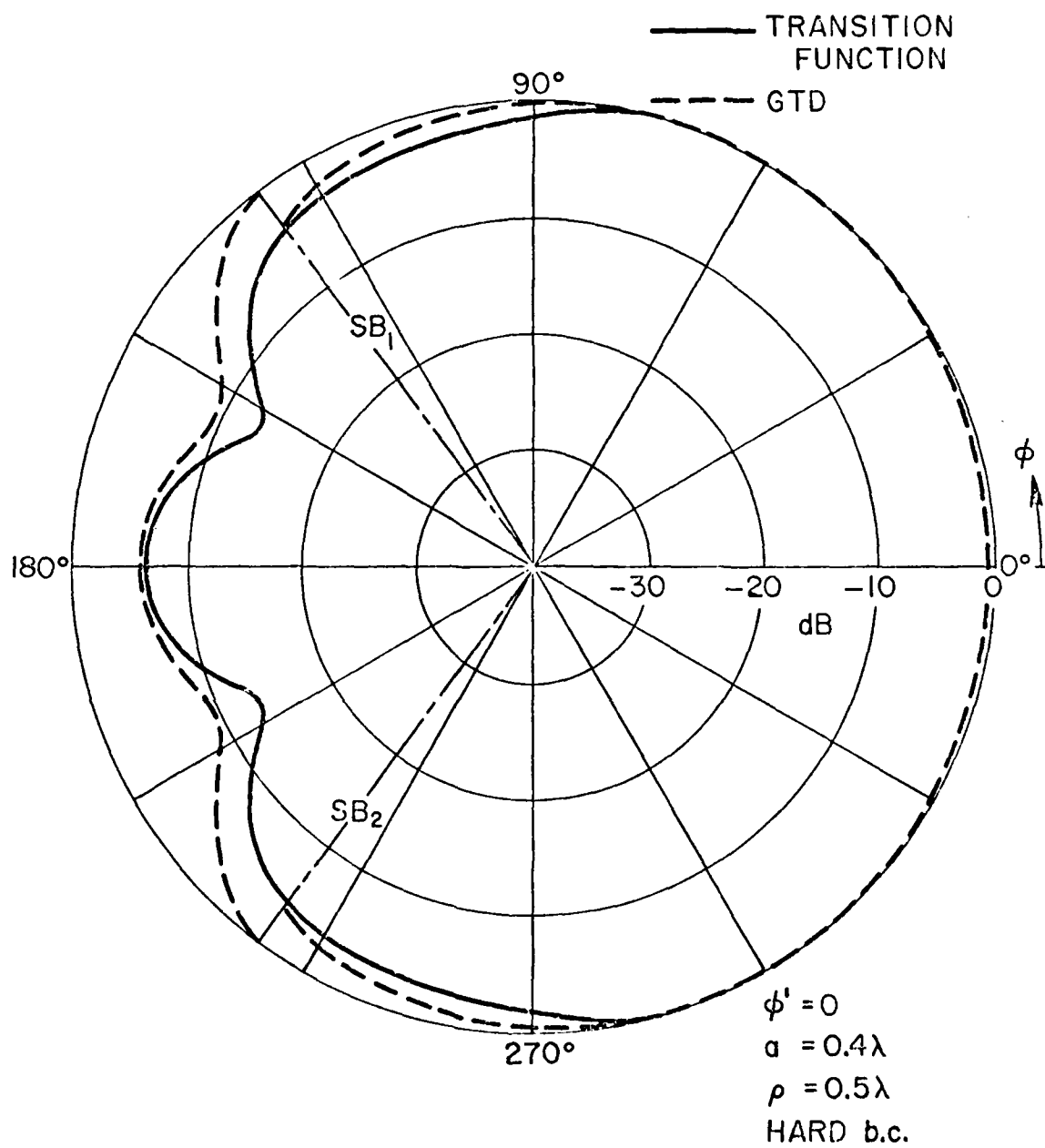


Fig. 12(a). Field surrounding a circular cylinder illuminated by a  $TE_z$  plane wave. Calculations based on GTD and the transition solution.

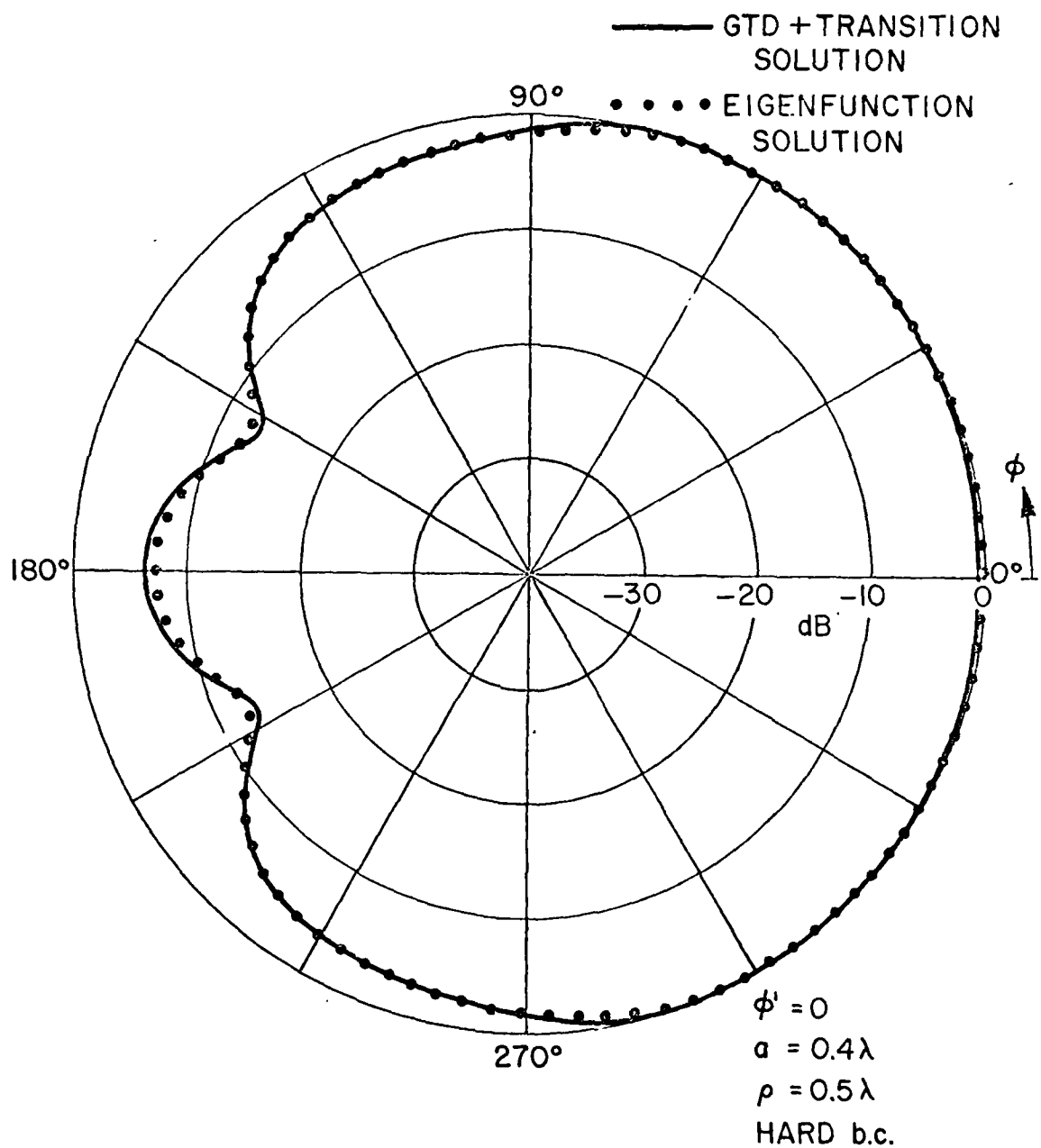


Fig. 12(b). Comparison of the composite GTD plus transition solution of Fig. 12(a) with the exact solution.

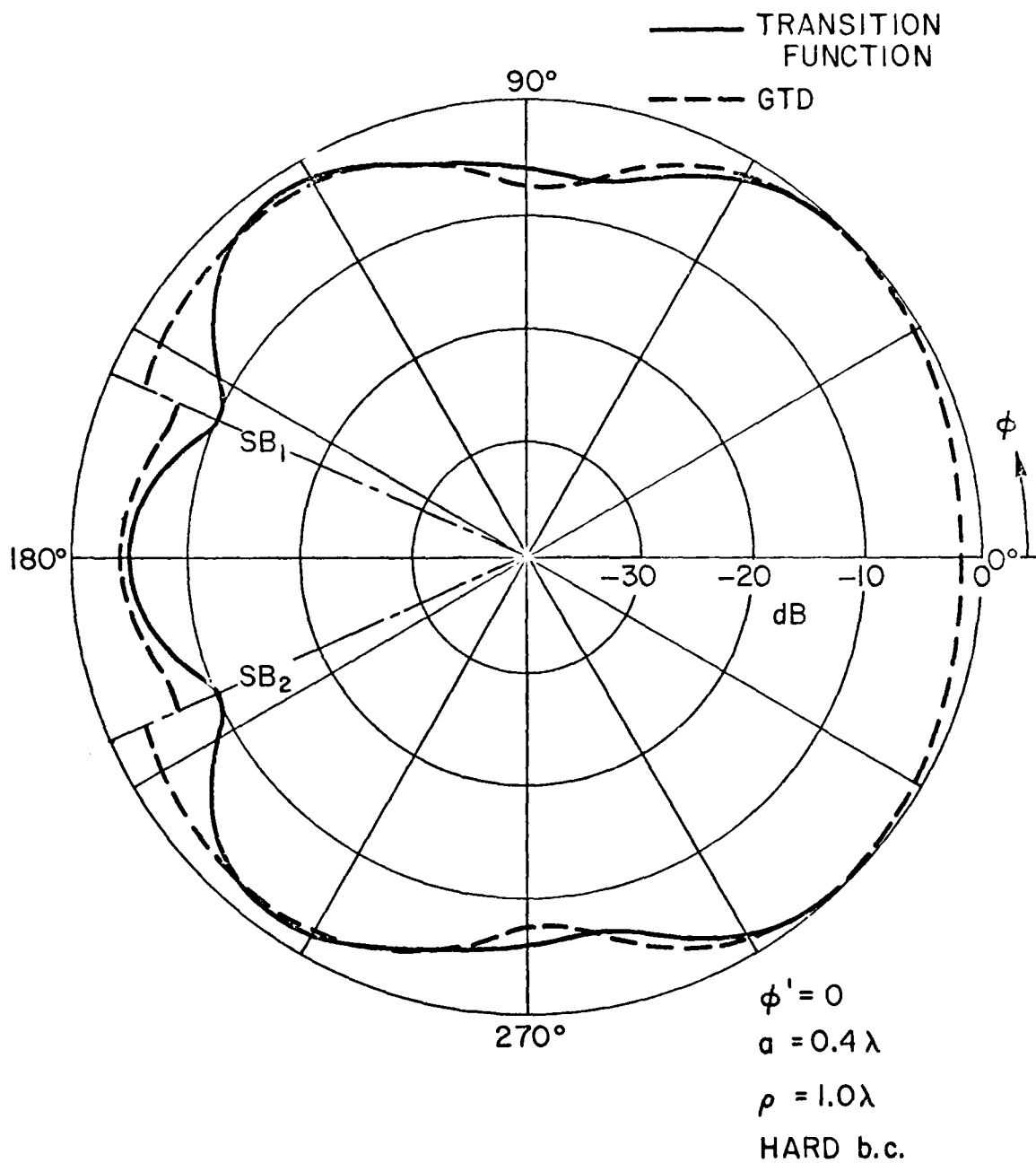


Fig. 13(a). Field surrounding a circular cylinder illuminated by a  $TE_z$  plane wave. Calculations based on GTD and the transition solution.

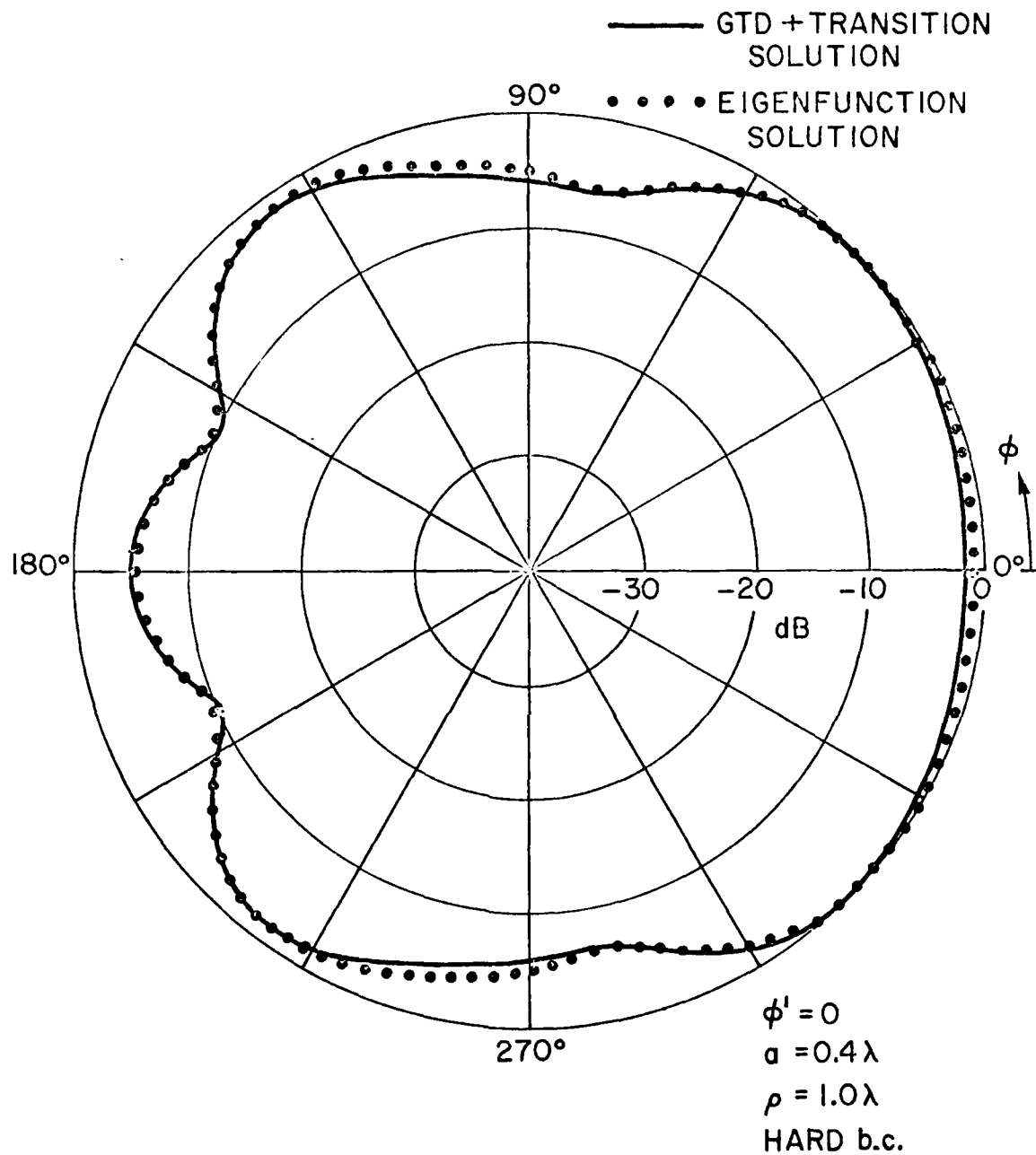


Fig. 13(b). Comparison of the composite GTD plus transition solution of Fig. 13(a) with the exact solution.



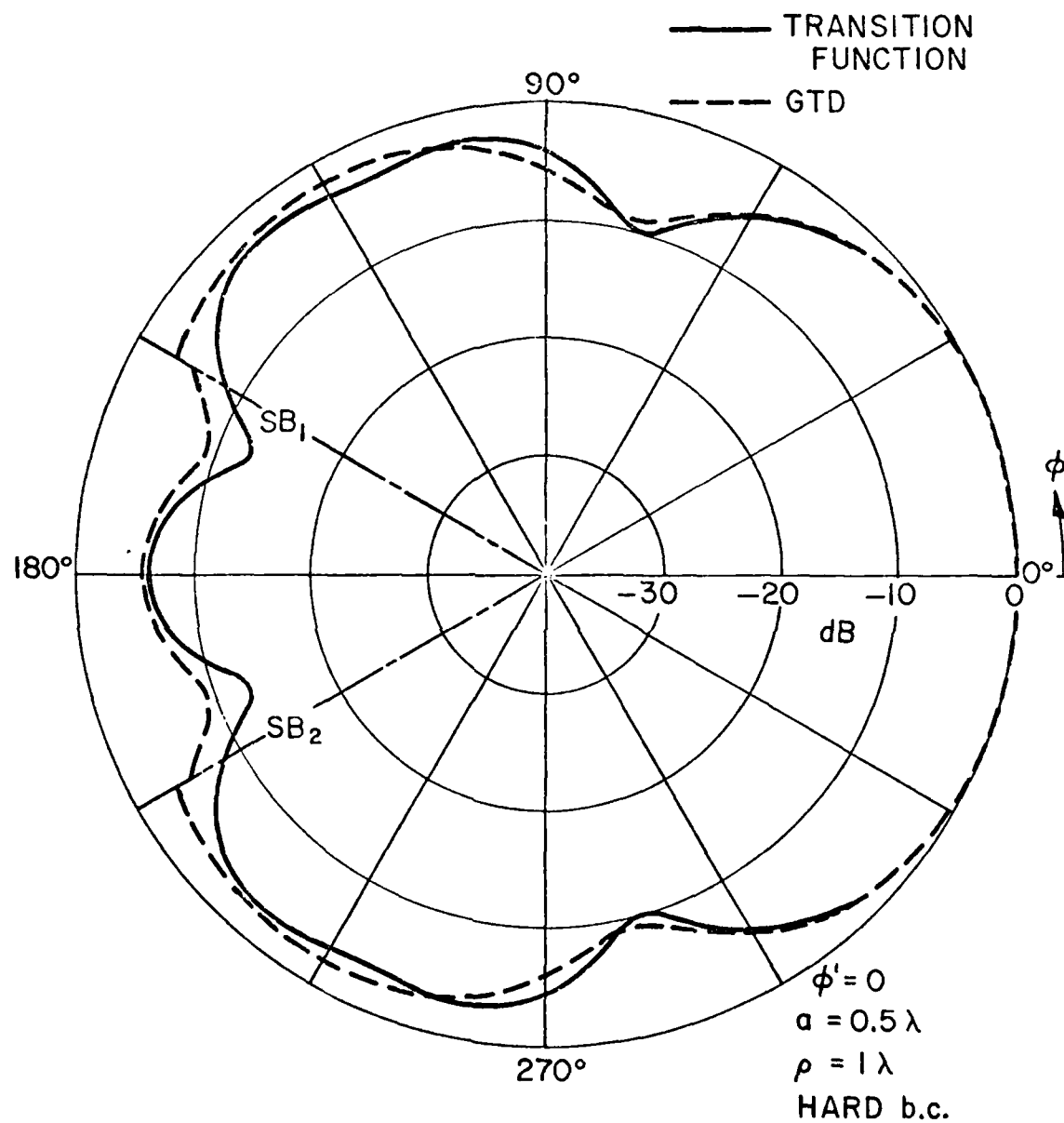


Fig. 14(a). Field surrounding a circular cylinder illuminated by a  $TE_z$  plane wave. Calculations based on GTD and the transition solution.

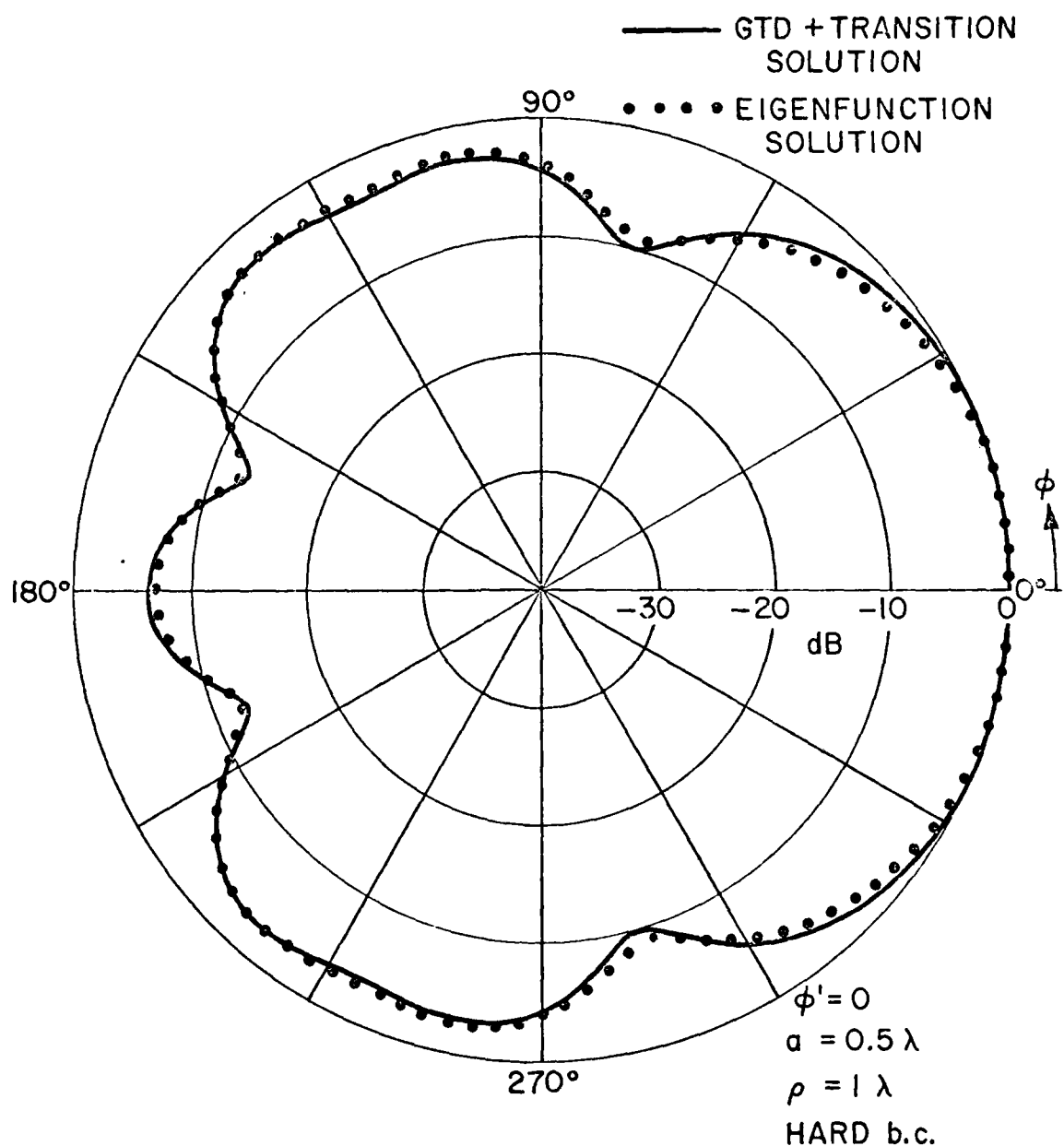


Fig. 14(b). Comparison of the composite GTD plus transition solution of Fig. 14(a) with the exact solution.

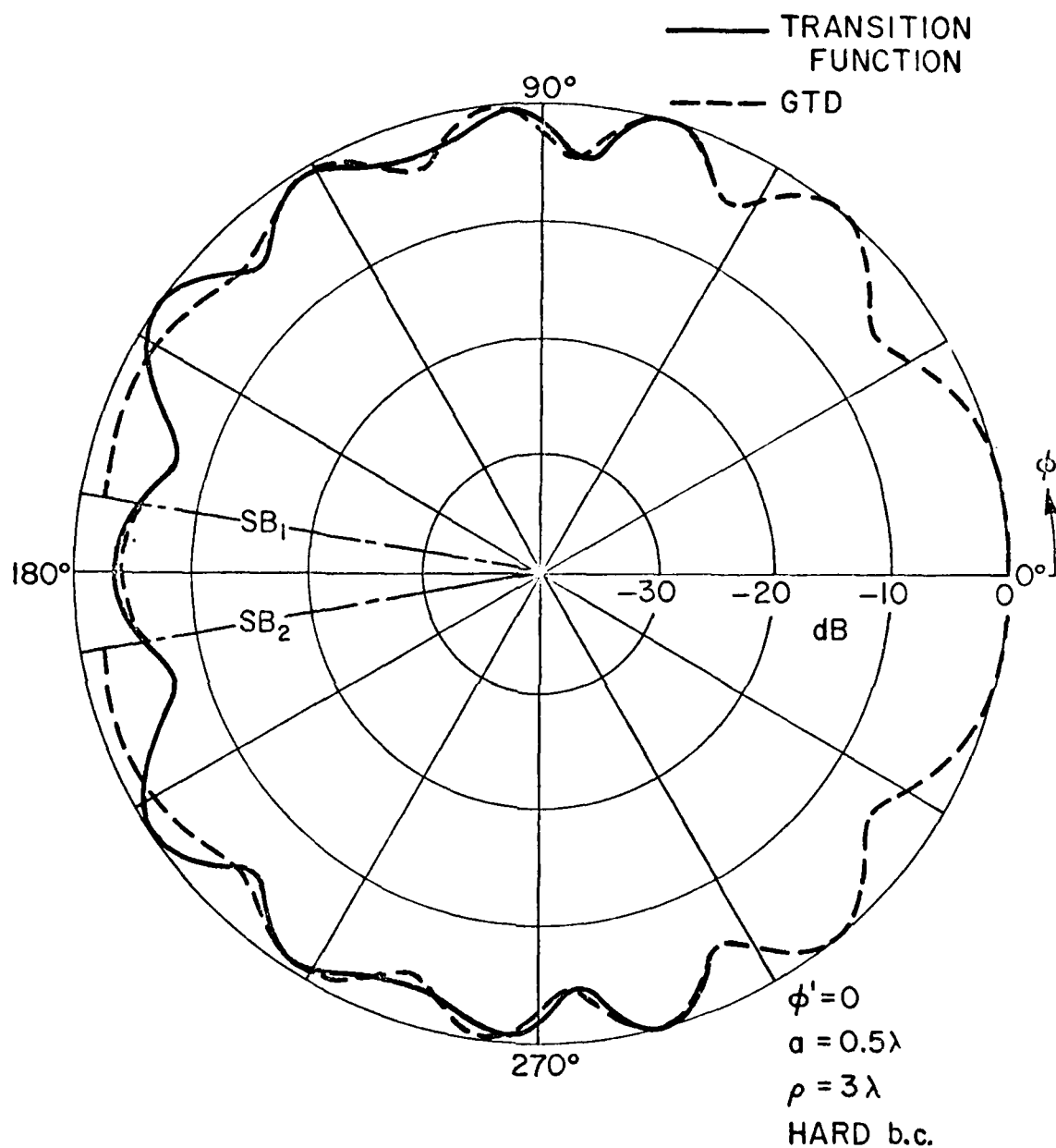


Fig. 15(a). Field surrounding a circular cylinder illuminated by a  $TE_z$  plane wave. Calculations based on GTD and the transition solution.

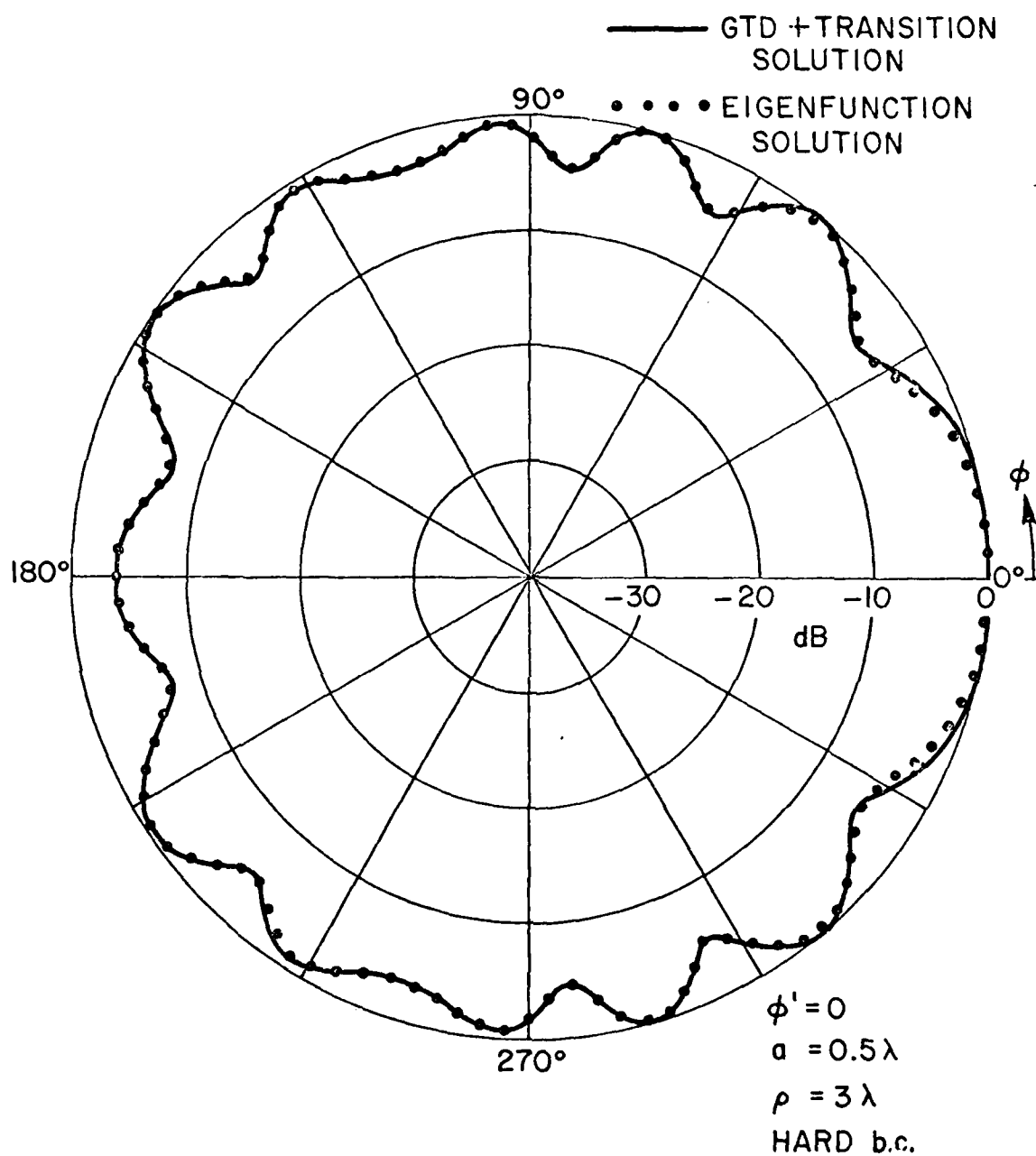


Fig. 15(b). Comparison of the composite GTD plus transition solution of Fig. 15(a) with the exact solution.

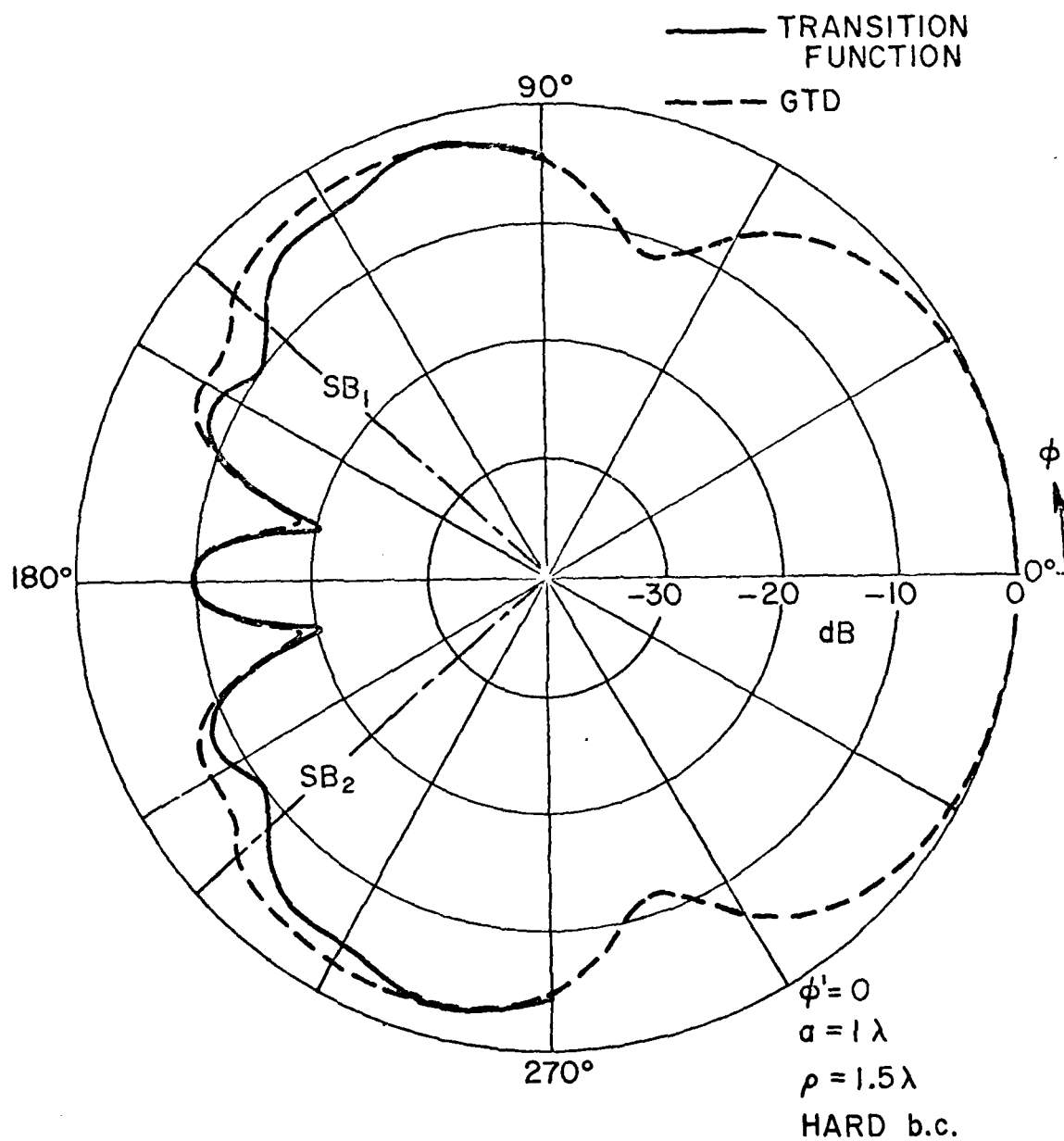


Fig. 16(a). Field surrounding a circular cylinder illuminated by a  $TE_z$  plane wave. Calculations based on GTD and the transition solution.

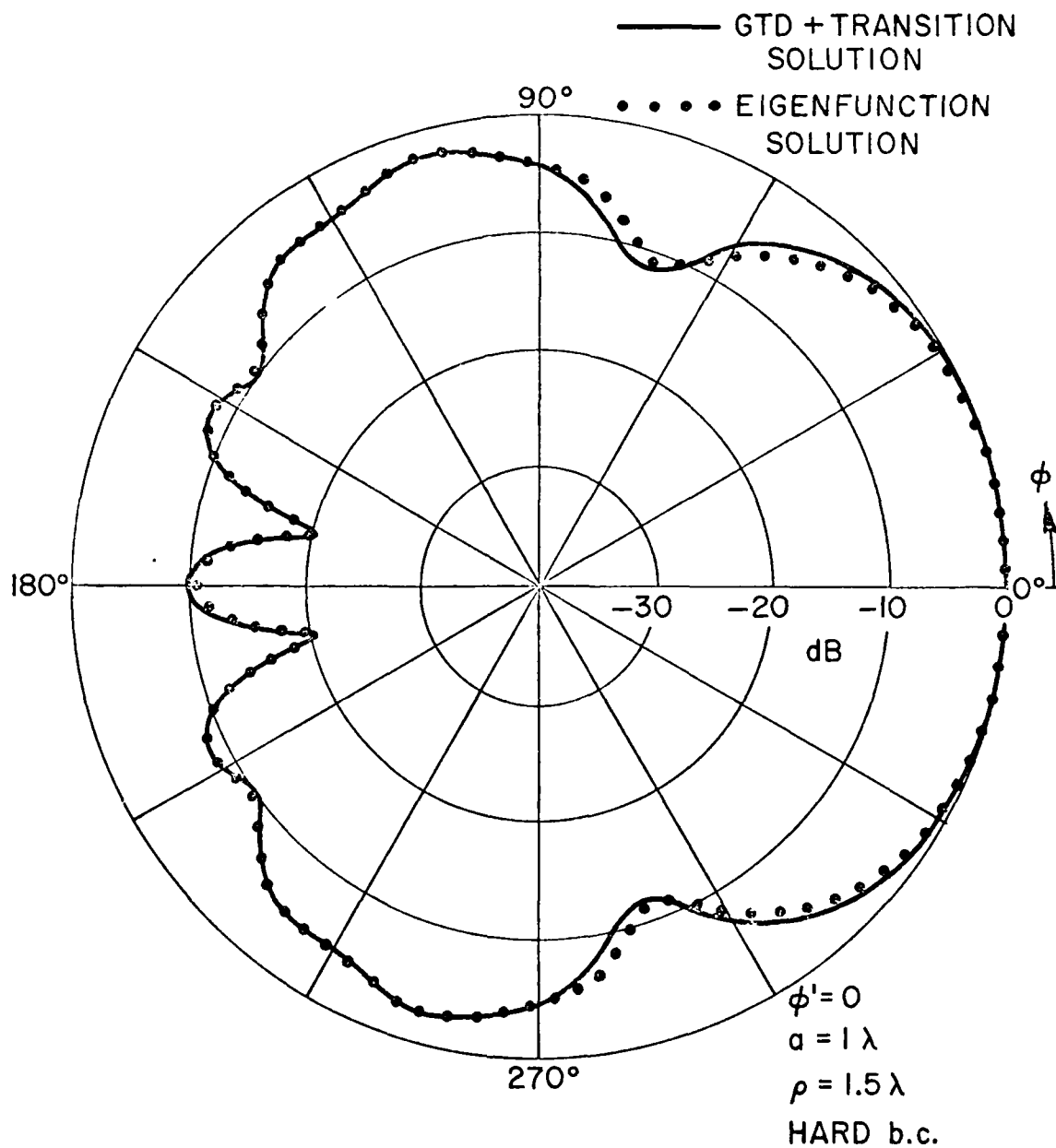


Fig. 16(b). Comparison of the composite GTD plus transition solution of Fig. 16(a) with the exact solution.

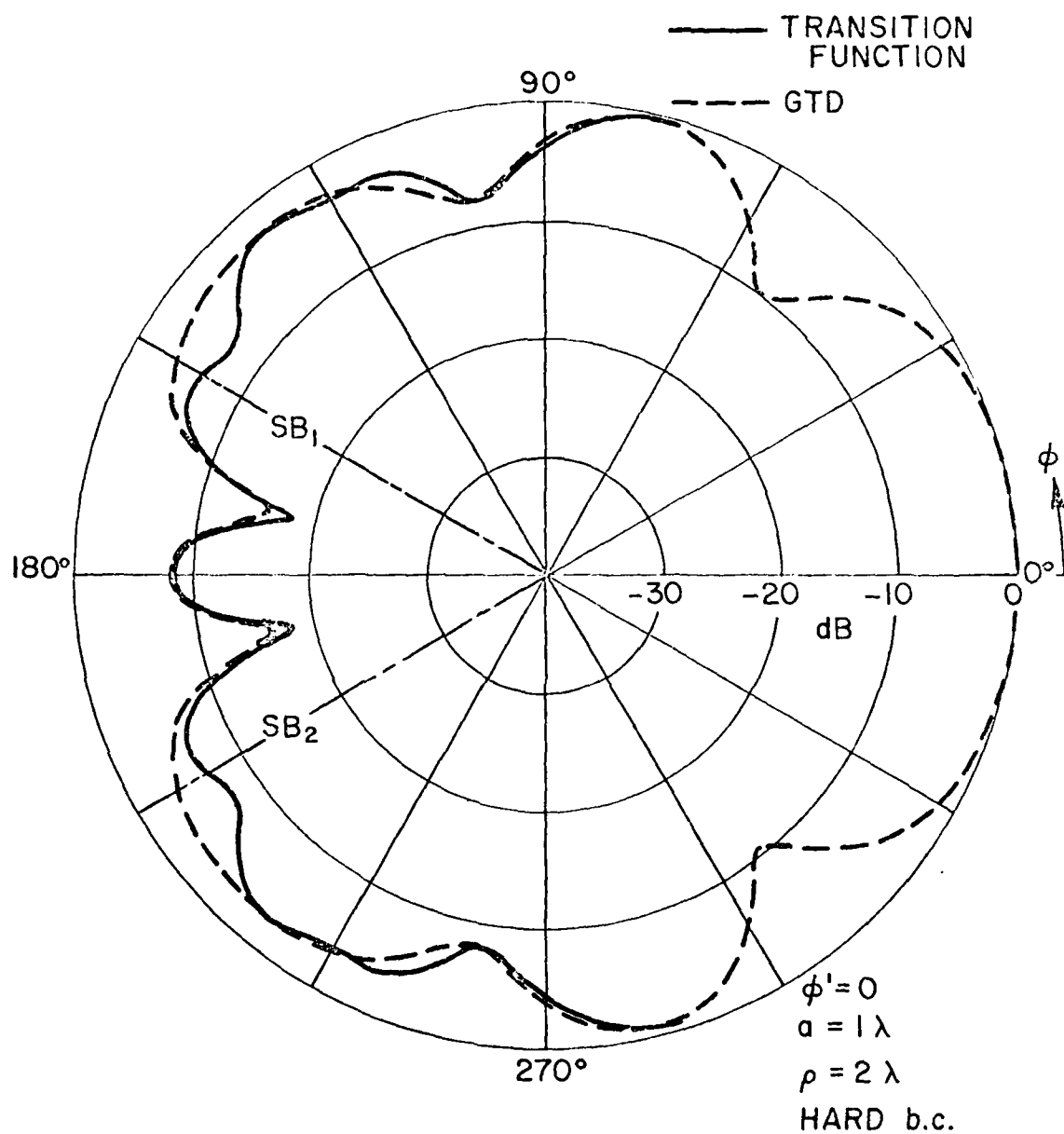


Fig. 17(a). Field surrounding a circular cylinder illuminated by a  $TE_z$  plane wave. Calculations based on GTD and the transition solution.

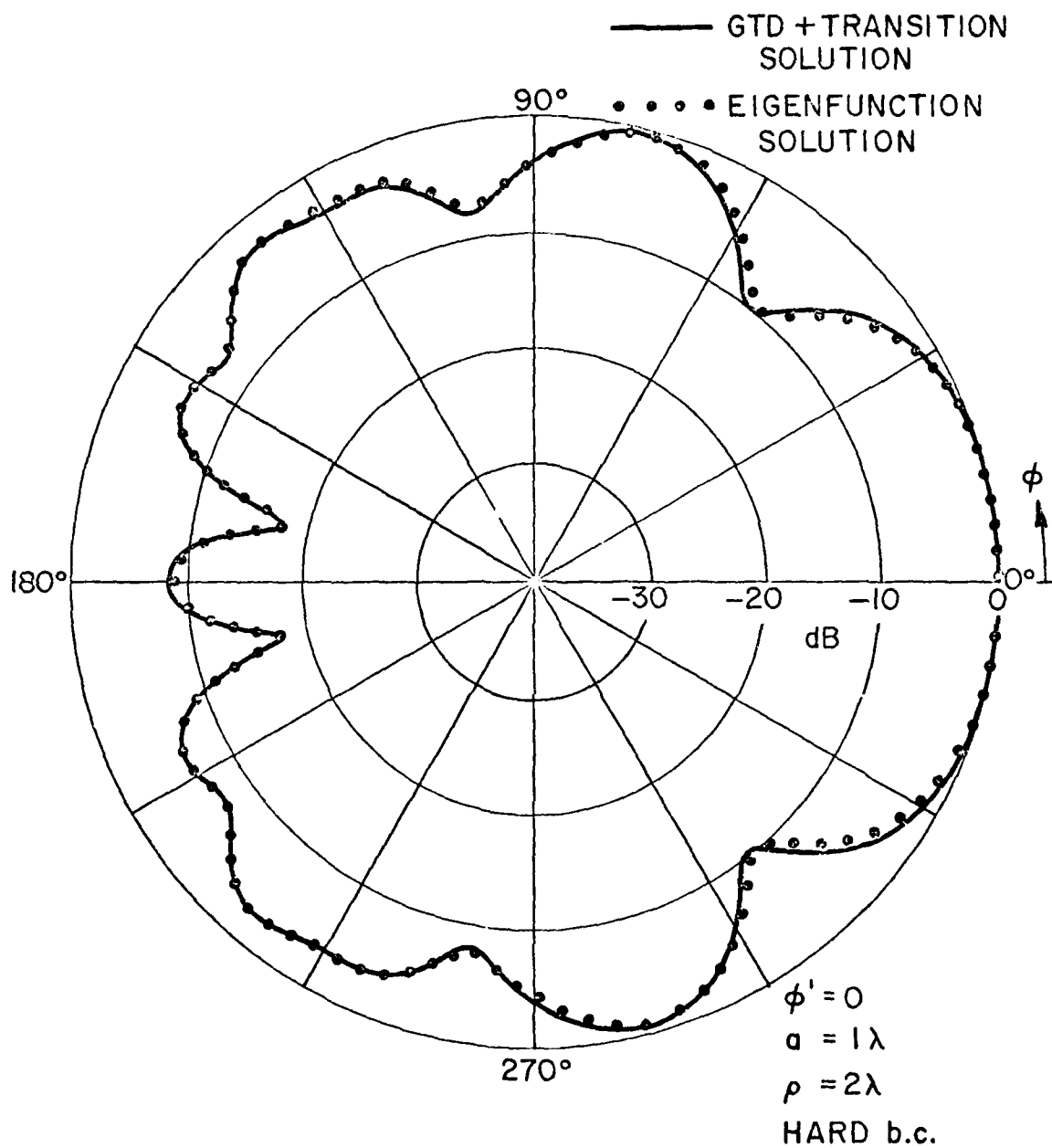


Fig. 17(b). Comparison of the composite GTD plus transition solution of Fig. 17(a) with the exact solution.



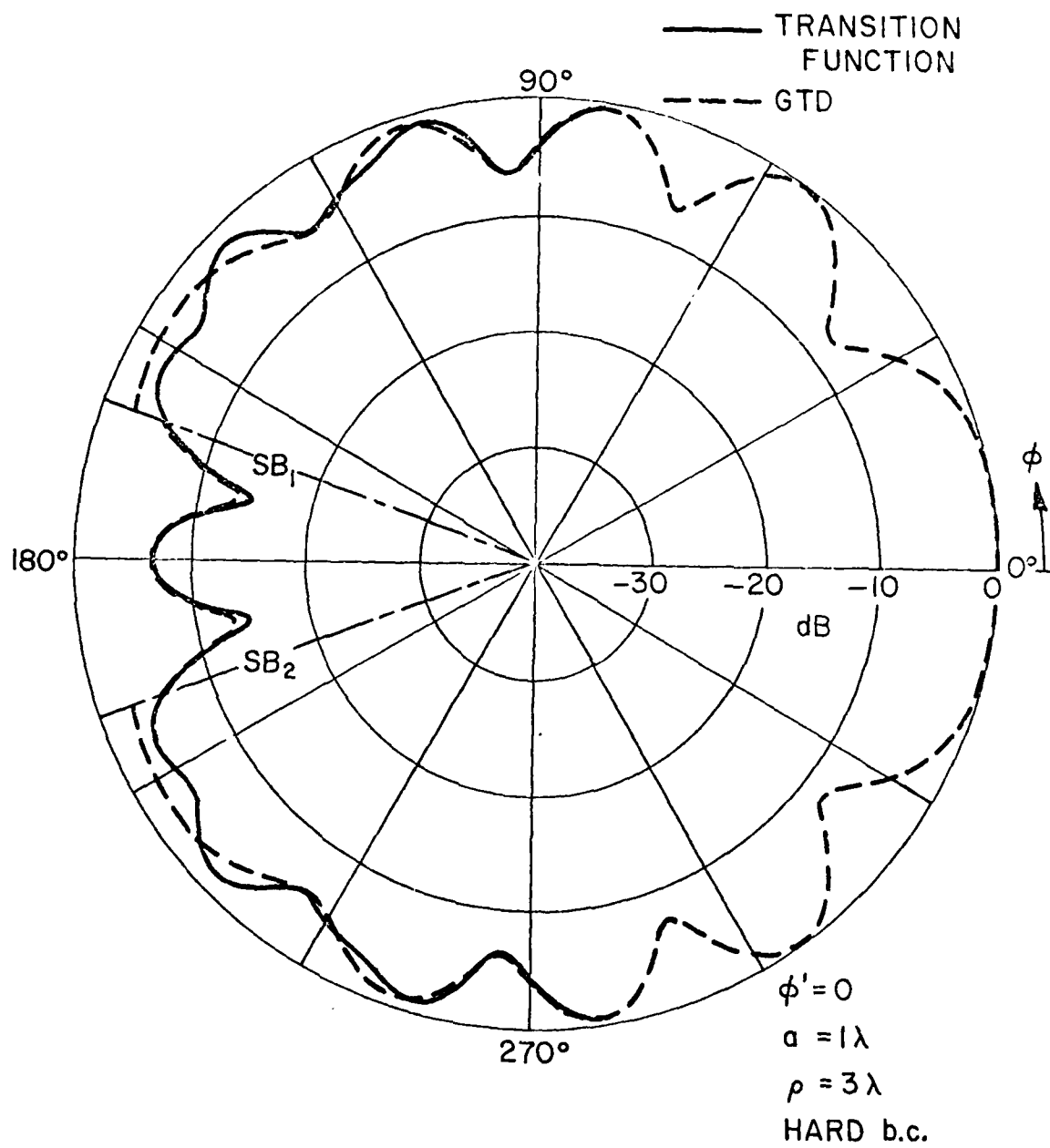


Fig. 18(a). Field surrounding a circular cylinder illuminated by a  $TE_z$  plane wave. Calculations based on GTD and the transition solution.

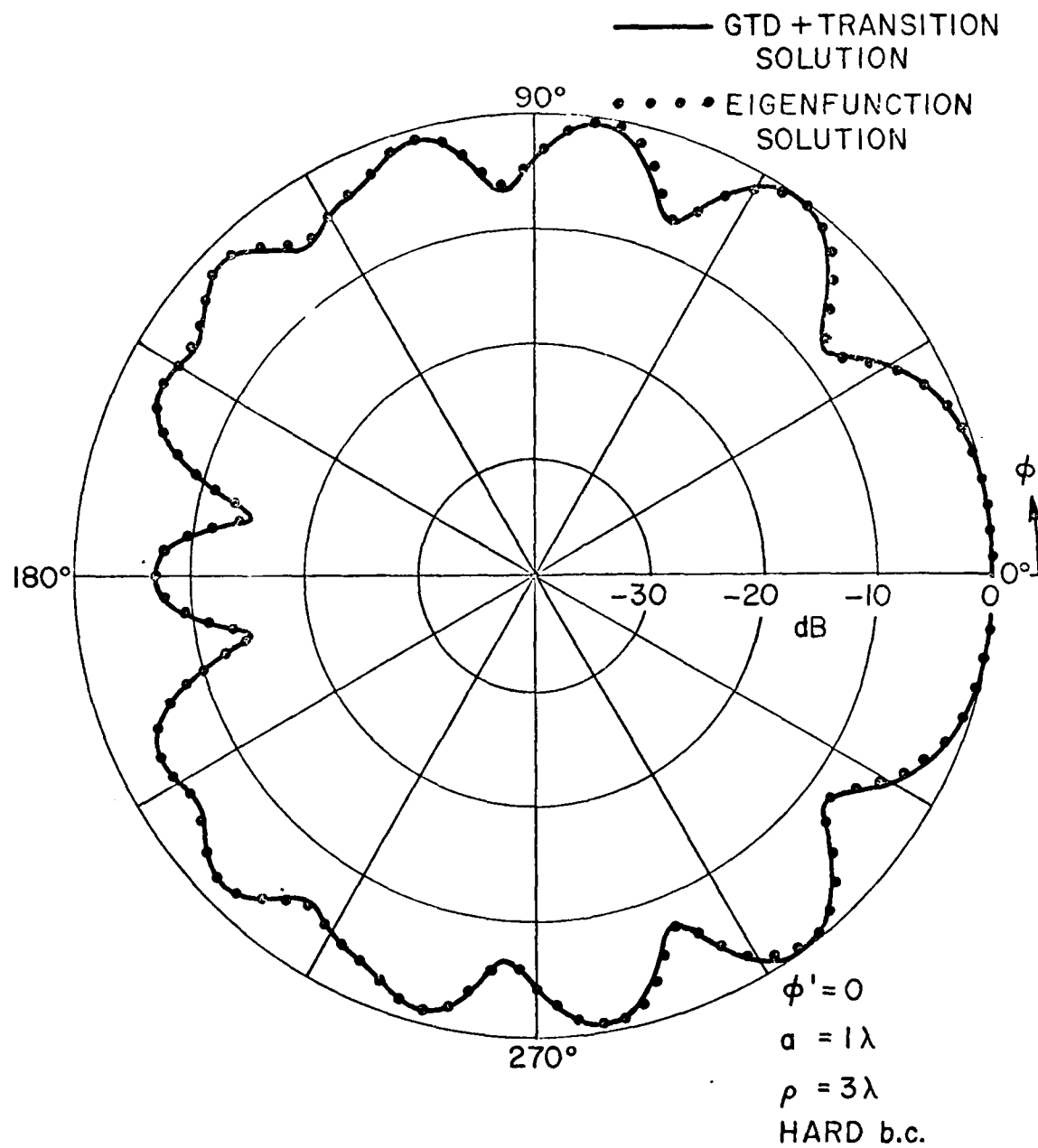


Fig. 18(b). Comparison of the composite GTD plus transition solution of Fig. 18(a) with the exact solution.

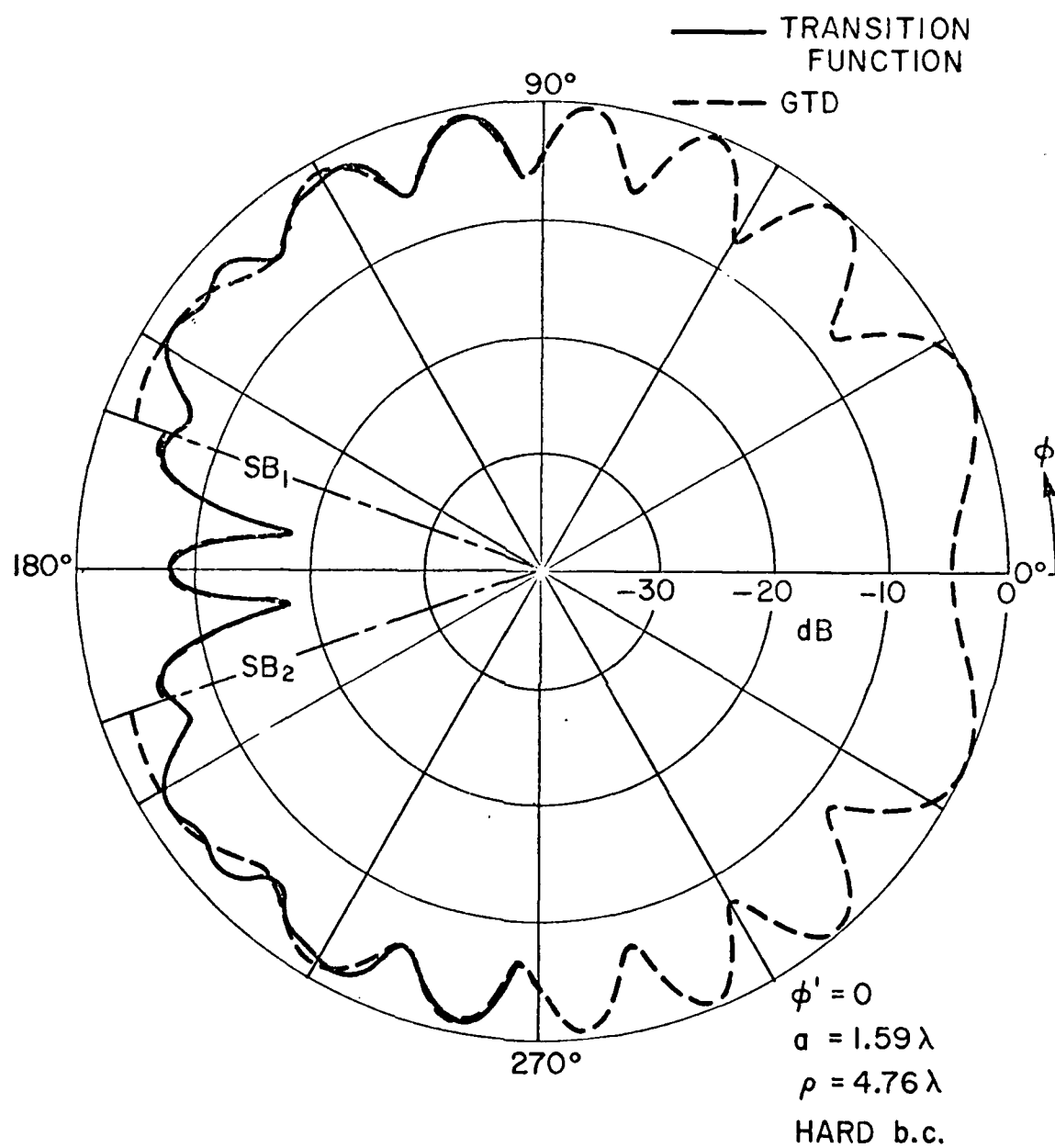


Fig. 19(a). Field surrounding a circular cylinder illuminated by a  $TE_z$  plane wave. Calculations based on GTD and the transition solution.

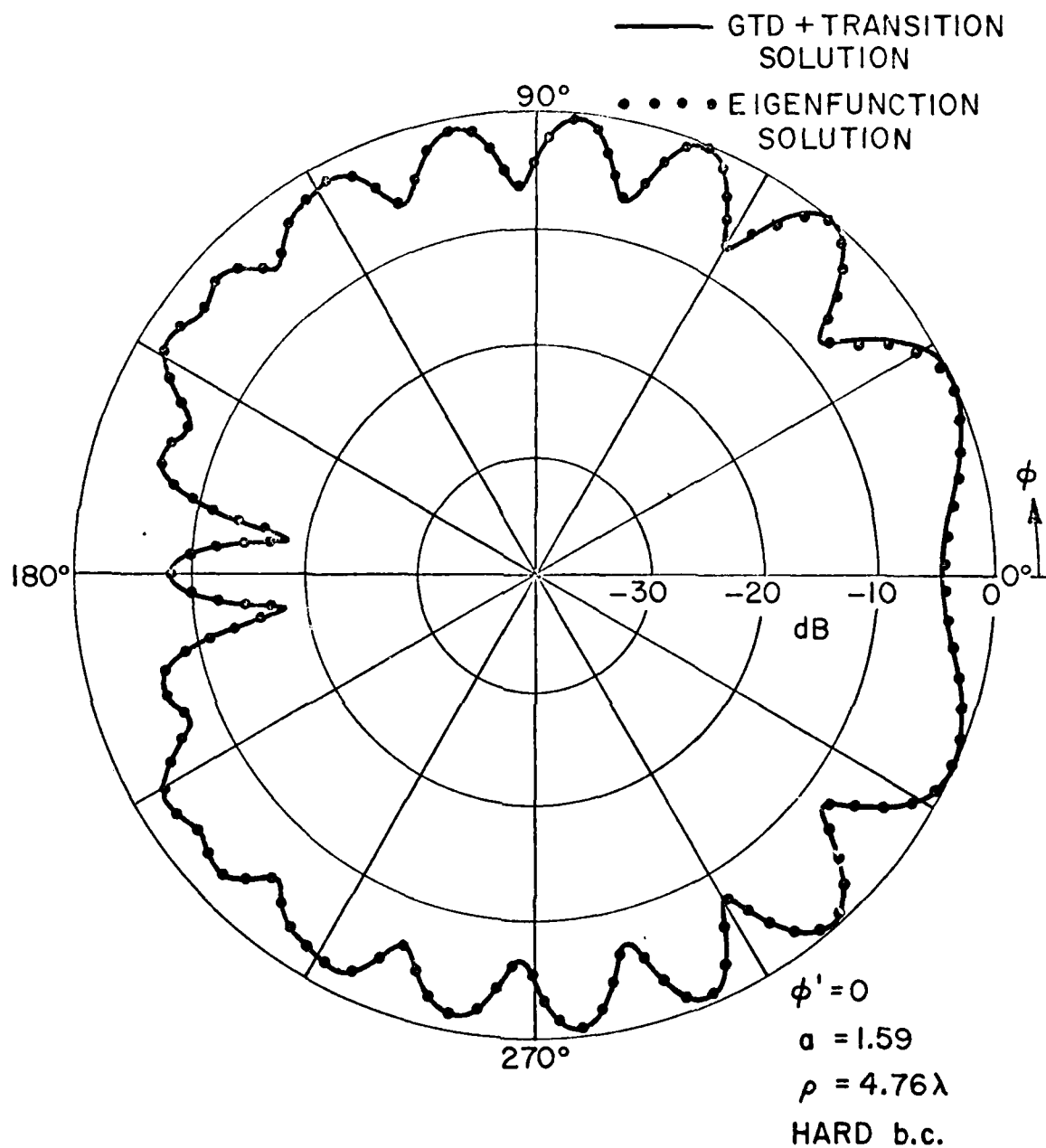


Fig. 19(b). Comparison of the composite GTD plus transition solution of Fig. 19(a) with the exact solution.

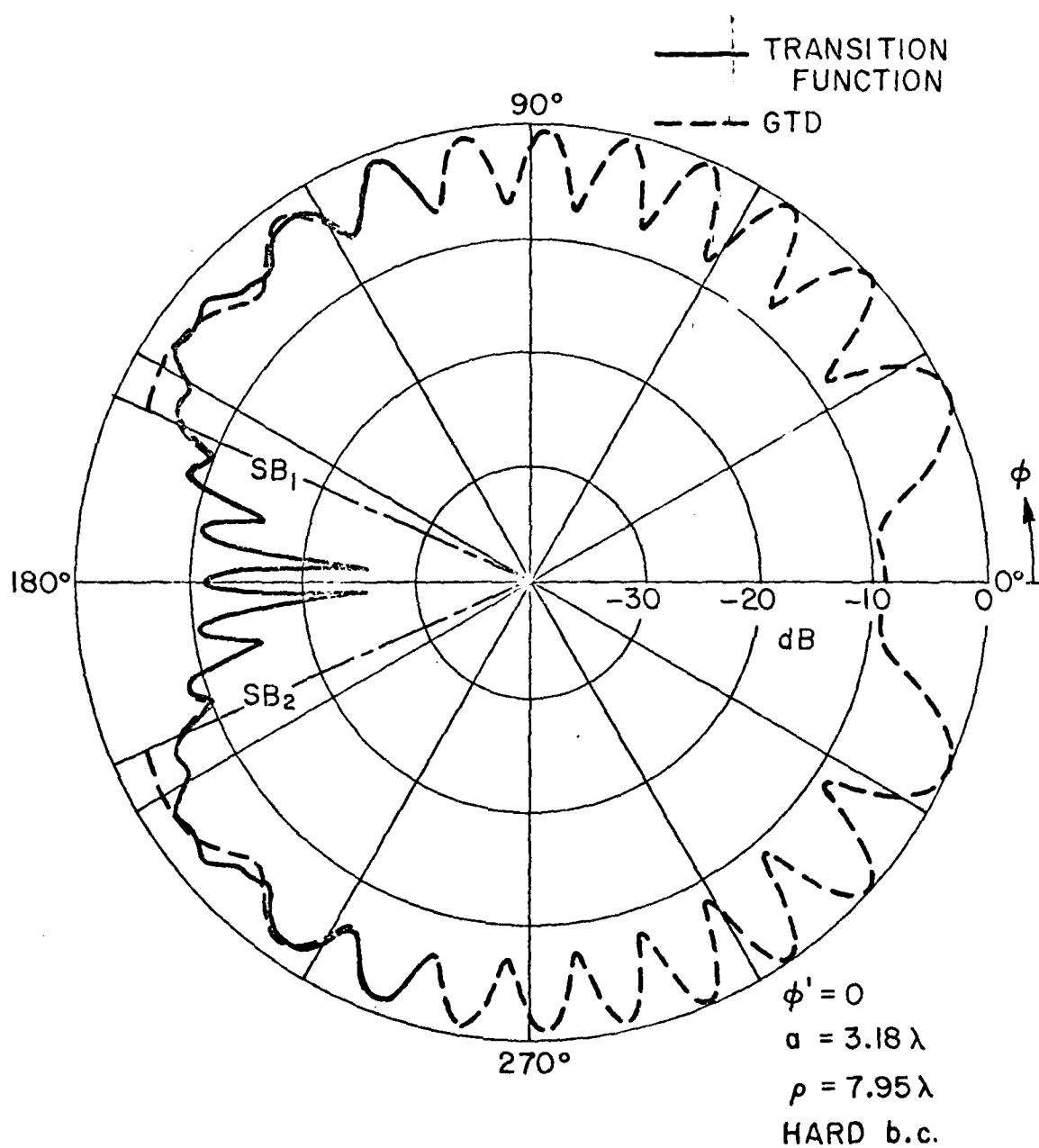


Fig. 20(a). Field surrounding a circular cylinder illuminated by a  $TE_z$  plane wave. Calculations based on GTD and the transition solution.

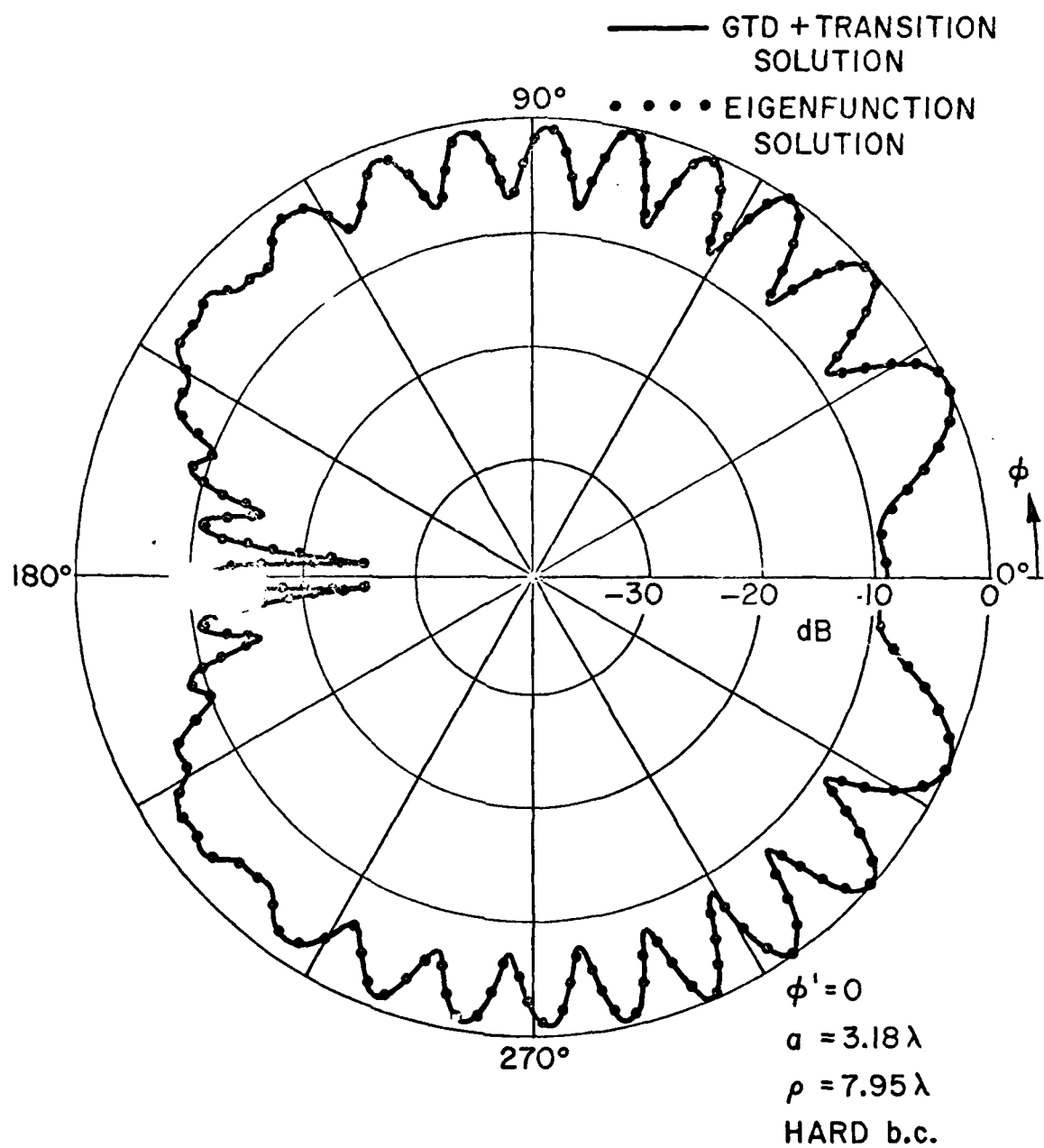


Fig. 20(b). Comparison of the composite GTD plus transition solution of Fig. 20(a) with the exact solution.

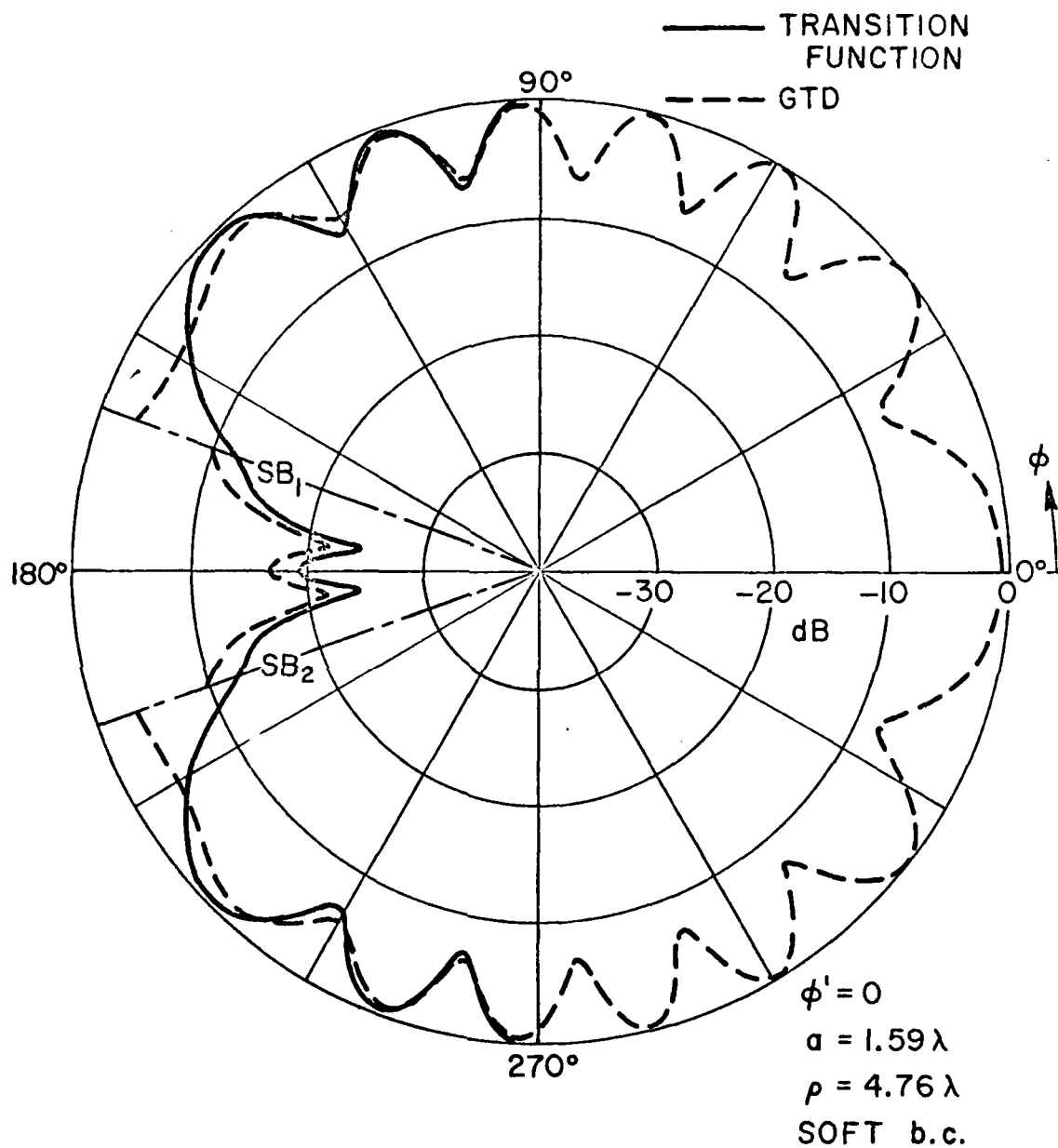


Fig. 21(a). Field surrounding a circular cylinder illuminated by a  $TM_z$  plane wave. Calculations based on GTD and the transition solution.

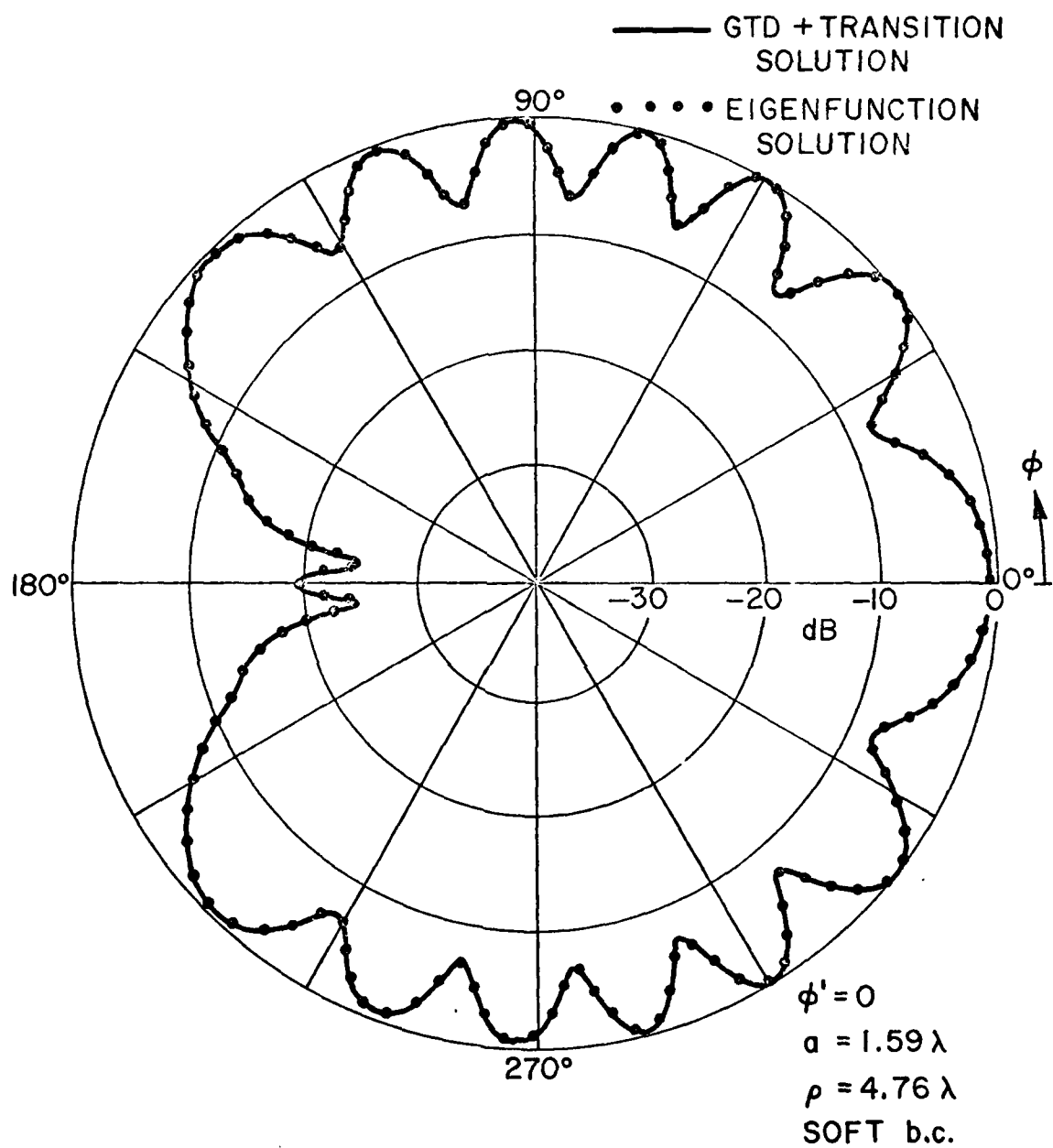


Fig. 21(b). Comparison of the composite GTD plus transition solution of Fig. 21(a) with the exact solution.



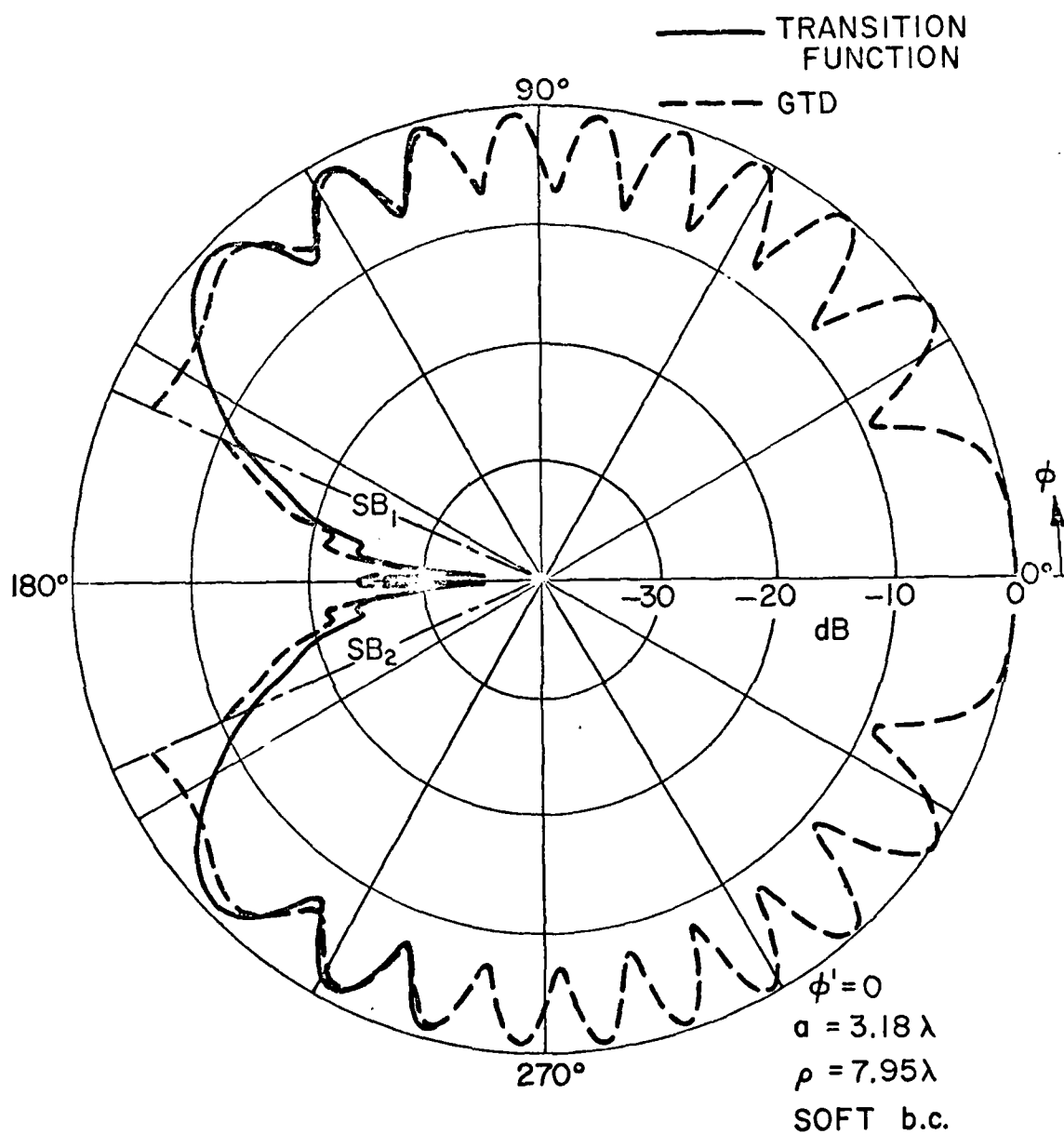


Fig. 22(a). Field surrounding a circular cylinder illuminated by a  $TM_z$  plane wave. Calculations based on GTD and the transition solution.

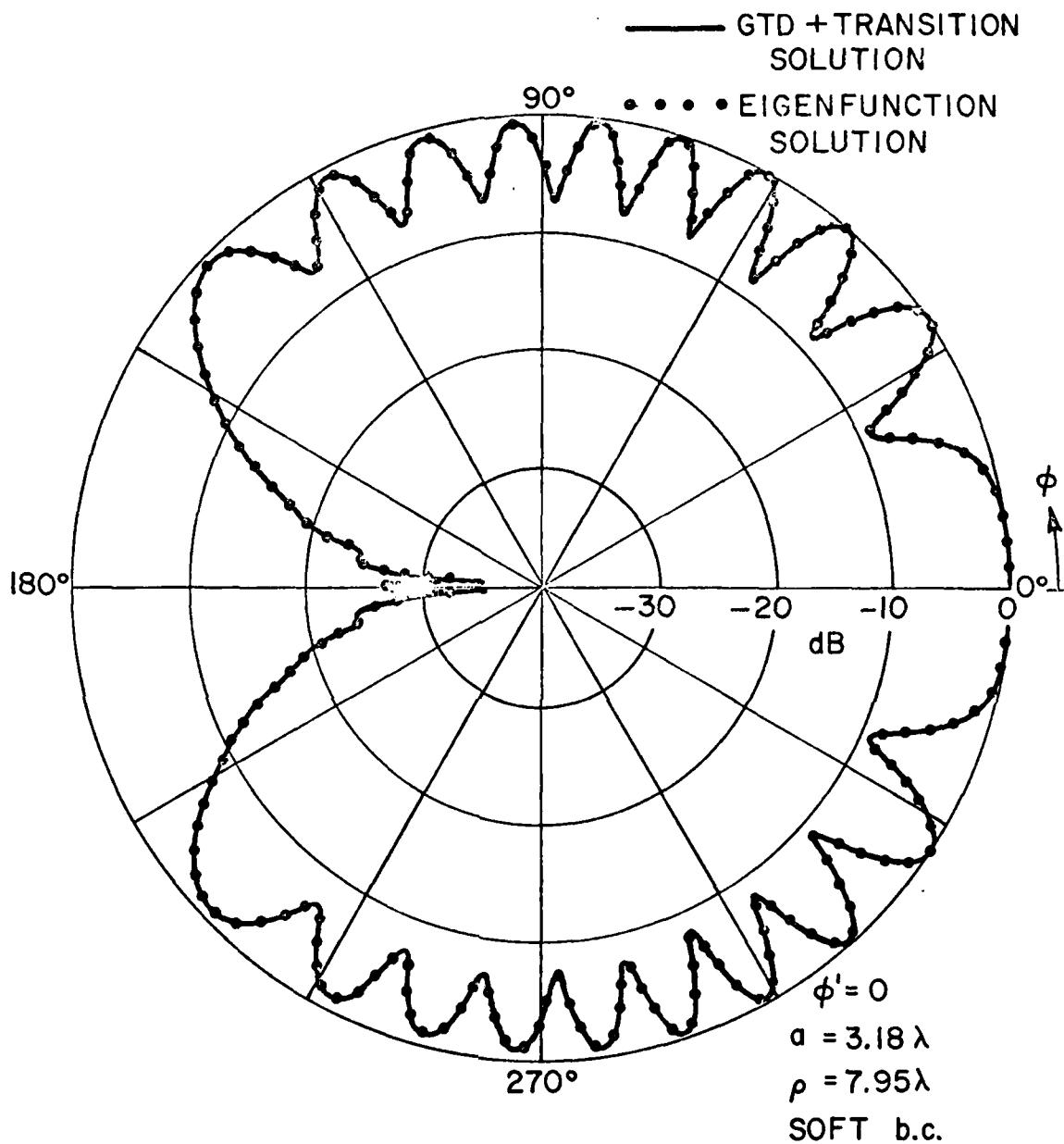


Fig. 22(b). Comparison of the composite GTD plus transition solution of Fig. 22(a) with the exact solution.

#### IV. SUMMARY AND DISCUSSION

A uniform asymptotic result is developed for describing the fields in the transition regions adjacent to the shadow boundaries which are associated with the problem of plane wave diffraction by a perfectly-conducting, circular cylinder. This result yields a finite, continuous solution for the total field across the shadow boundaries, and exterior to the transition regions it reduces to the usual GTD solution (in terms of the surface diffracted fields and geometrical optical ray fields) for the shadow and lit zones, respectively.

Summarizing this result for convenience, one expresses the total field  $U$  exterior to the cylinder via (27) and (49) as

##### TRANSITION REGION - SHADOW ZONE

$$(51a) \quad U(P_S) \sim U^i(Q_1) \left[ -m \sqrt{\frac{2}{k}} \left( \hat{P}_S(\xi) + \frac{e^{-i\frac{\pi}{4}}}{2\sqrt{\pi\xi}} \left\{ 1 - F \left[ k s \frac{\xi^2}{2m^2} \right] \right\} \right) \right] e^{-ikt} \frac{e^{-iks}}{\sqrt{s}} ;$$

with  $\xi = m\theta > 0$ ,

where  $t = a\theta = Q_1 Q_2$ ,  $s = Q_2 P_S$  as in Fig. 7; and  $m = \left( \frac{ka}{2} \right)^{1/3}$ . The functions  $F[k s \frac{\xi^2}{2m^2}]$  and  $\hat{P}_S(\xi)$  are tabulated in Figs. 6 and 8,

respectively; one should note that  $\hat{P}_S(\xi)$  is associated with the acoustic soft boundary case ( $TM_z$ ), and  $\hat{P}_h(\xi)$  is associated with the acoustic hard boundary case ( $TE_z$ ). Also,  $U^i(Q_1)$  denotes the value of the incident field at  $Q_1$ .

##### TRANSITION REGION - LIT ZONE

$$(51b) \quad U(P_L) \sim U^i(P_L) + U^i(Q_R) \left[ -m \sqrt{\frac{2}{k\rho_r}} e^{-i\frac{(\xi')^3}{12}} \cdot \left( \hat{P}_S(\xi') + \frac{e^{-i\frac{\pi}{4}}}{2\sqrt{\pi\xi'}} \left\{ 1 - F \left[ k\ell \frac{\xi'^2}{2m^2} \right] \right\} \right) \right] \sqrt{\frac{\rho_r}{\rho_r + \ell}} e^{-ik\ell} ;$$

with  $\xi' = -2m \cos \theta^i < 0$ ,

where  $\ell = Q_R P_L$ ,  $\rho_r = \frac{a \cos \theta^i}{2}$ ; and  $m$ ,  $F[k\ell \frac{\xi'^2}{2m^2}]$ ,  $\hat{P}_S(\xi')$ ,

and  $U^i$  have the same meaning as before. The geometrical quantities  $\lambda, \theta^i$  and the point of reflection  $Q_R$  are indicated in Fig. 11. One

notes that  $\hat{P}_S(\xi) + \frac{e^{-i\frac{\pi}{4}}}{2\sqrt{\pi} \xi} = \begin{cases} p^*(\xi) \\ q^*(\xi) \end{cases} e^{-i\frac{\pi}{4}}$  in (51a) and (51b),

respectively. The functions  $p^*$  and  $q^*$  are plotted in Fig. 8.

Equation (51) is valid for both, the near and the far zone; however, in the near zone case, the field point must lie exterior to the surface boundary layer. Within the surface boundary layer, (51a) tends to become singular (as  $s \rightarrow 0$ ) in exactly the same manner as the GTD surface diffracted ray field of (33) which becomes singular as  $s \rightarrow 0$ . In order to remove this limitation, one must employ (39) instead of (23) in the analysis as  $s \rightarrow 0$ ; however, the case  $s \rightarrow 0$  is not considered in this paper. One could employ the results of Ivanov [11] which allows the field to be calculated near the surface (within the surface boundary layer) as  $s \rightarrow 0$ . However, as mentioned earlier, his result [11] is in terms of the canonical Fock integral which is complicated for numerical calculations except at  $s=0$ ; when  $s=0$ , the canonical Fock integral reduces to the single parameter Fock current integral which is well tabulated. It would be worth investigating an alternative approximate solution which matches our solution of (51) outside the surface boundary layer, but which reduces to the Fock currents on the surface ( $s=0$ ), and at the same time is such that it is simple for numerical processing.

The result in (51) yields a finite and continuous field solution across the shadow boundaries. Away from the shadow boundaries, and exterior to the transition region (51a) reduces to the GTD surface diffracted ray field of (33); whereas, (51b) reduces to the geometrical optics incident and reflected ray fields of (37). The  $F[\cdot]$  term in (51) dominates in the region at and near the shadow boundaries; whereas, far from the shadow boundaries the  $\hat{P}_S(\cdot)$  term dominates.

Since the  $F(\cdot)$  and  $\hat{P}_S(\cdot)$  functions are well tabulated [9], the result in (51) is simple to use which makes it well suited to solve practical problems. Furthermore, this result can be readily generalized to convex surfaces of variable curvature in both two and three dimensions by employing the local nature of high frequency fields and reciprocity. These extensions will be presented in a separate paper. Finally, the field at  $(\rho, \phi)$  due to  $TM_z$  (or  $TE_z$ ) plane wave scattering by the cylinder is directly related via reciprocity to the problem of calculating the radiation pattern (along the incident field direction) of an electric (or magnetic) line source at  $(\rho, \phi)$  in the presence of the same cylinder; the latter problem is of interest for estimating the radiation patterns of antennas mounted off the fuselage of a typical aircraft.

# REFERENCES

- [1] Keller, J. B., "Proceedings of Symposium on Microwave Optics," Part II, McGill University, 1953, pp. 207-210 (AD 211500).
- [2] Keller, J. B., "Geometrical Theory of Diffraction," J. Opt. Soc. Am., Vol. 52, No. 2, 1962, pp. 116-130.
- [3] Keller, J. B., "Diffraction by a Convex Cylinder," Trans. I.R.E., Vol. AP-24, 1956, pp. 312-321.
- [4] Burnside, W. D., "Analysis of On-Aircraft Antenna Patterns," Report 3390-1, August 1972, The Ohio State University Electro-Science Laboratory, Department of Electrical Engineering; prepared under Contract N62269-72-C-0354 for Naval Air Development Center.
- [5] Burnside, W. D., Gilreath, M. C., Marhefka, R. J., and Yu, C. L., "A Study of KC-135 Aircraft Antenna Pattern," IEEE Trans. AP-5, May 1975, pp. 309-316.
- [6] Fock, V. A., Diffraction, Refraction and Reflection Waves: Thirteen Papers, Air Force Cambridge Research Center Report AFCRC-TN-57-T02, June 1957 (AD 117276).
- [7] Fock, V. A., "Fresnel Diffraction from Convex Bodies," Uspekii Fizicheskikh Nauk., Vol. 43, 1951, pp. 587-599. (Also in Ref. [6].)
- [8] Wait, J. R., and Conda, A. M., "Diffraction of Electromagnetic Waves by Smooth Obstacles," Jour. of Res., N.B.S., Vol. 63D, No. 2, Sept.-Oct., 1959, pp. 181-197.
- [9] Logan, N. A., "General Research in Diffraction Theory," Vol. I, LMSD-288087; and Vol. II, LMSD-288088, Missiles and Space Division, Lockheed Aircraft Corp., Dec. 1959.
- [10] Logan, N. A., and Yee, K. S., Electromagnetic Waves, Edited by R. E. Langer, Univ. of Wisconsin Press, 1962.
- [11] Ivanov, V. I., U.S.S.R. Journal of Computational Math. and Math. Phys. (Translated from Zl. Vychisl. Mat. Mat. Fiz.), Vol. 2, 1971, p. 216.
- [12] Borovikov, V. A., and Kinber, B. Y., Proc. IEEE, Vol. 62, No. 11, Nov. 1974, pp. 1416-1437.
- [13a] Fock, V. A., "The Field of a Plane Wave Near the Surface of a Conducting Body," Izvestia Akademii Nauk (ser. Fiz.), Vol. 10, 1946, p. 171 (also in [6]).

- [13b] Fock, V. A., "The Field of a Vertical and Horizontal Dipole Raised Above the Earth's Surface," J. Exp. Theor. Phys. (ZETF), Vol. 19, 1949, p. 916 (also in [6]).
- [14] Goriainov, A. S., Radio Eng. Electron (USSR), Vol. 3, 1958, p. 23 (transl. from Radiotechn. i Elektron, Vol. 3, p. 603, 1958).
- [15] Felsen, L. B., and Marcuvitz, N., Radiation and Scattering of Waves, Prentice Hall, Inc., Englewood Cliffs, N.J., 1973.
- [16] Clemmow, P. C., The Plane Wave Spectrum Representation of Electromagnetic Fields, Pergamon Press, Vol. 12 of Intl. Series of Monographs in Electromagnetic Waves, 1966.
- [17] Pathak, P. H., and Kouyoumjian, R. G., "The Dyadic Diffraction Coefficient for a Perfectly-Conducting Wedge," Report 2183-4, June 1970, The Ohio State University ElectroScience Laboratory, Department of Electrical Engineering; prepared under Contract AF 19(628)-5929 for Air Force Cambridge Research Laboratory.
- [18] Kouyoumjian, R. G., and Pathak, P. H., Proc. IEEE, Vol. 62, No. 11, Nov. 1974, pp. 1448-1461.

## APPENDIX

The result for the geometrical optics field reflected from a perfectly-conducting cylinder which is illuminated with a plane wave is developed in this Appendix; this development is useful to the analysis of section II B. Although this development is available in many texts (e.g., [15]), it is rederived here in terms of the notation employed in section II so that the connection between the results derived here with the analysis in section II B may be established in a convenient fashion. Only the  $TM_z$  case is treated here; the results for the  $TE_z$  case are exactly the same except for a change of sign.

Referring to Fig. 2, it is seen that the total field exterior to the cylinder in this case is (see (6b)):

$$(A1) \quad U \approx \frac{1}{2} \int_{-\infty-i\epsilon}^{\infty-i\epsilon} dv \left[ H_v^{(1)}(k\rho) - \frac{Q H_v^{(1)}(ka)}{Q H_v^{(2)}(ka)} H_v^{(2)}(k\rho) \right] e^{-iv[|\phi| - \frac{\pi}{2}]}.$$

For the  $TM_z$  case,  $Q = 1$ , and the first term on the RHS of (A1) yields the incident field [15]; on the other hand, the second term on the RHS of (A1) yields the reflected field for  $v < ka$ . One is concerned only with this second term which is denoted below by  $U_r$

$$(A2) \quad U_r \equiv -\frac{1}{2} \int_{-\infty-i\epsilon}^{\infty-i\epsilon} \frac{H_v^{(1)}(ka)}{H_v^{(2)}(ka)} H_v^{(2)}(k\rho) e^{-iv[|\phi| - \frac{\pi}{2}]} dv.$$

Employing the Debye approximations in the Hankel functions leads to:

$$(A3) \quad U_r \approx -\frac{1}{2} \int_{\gamma}^{\gamma} e^{-i\frac{\pi}{4}} e^{ik[2a \sin \tilde{\gamma} - (\frac{2v}{k} \tilde{\gamma}) - \rho \sin \gamma + \frac{v}{k} \gamma - \frac{v}{k} \psi]} \cdot \sqrt{\frac{2}{\pi k \rho \sin \gamma}} dv,$$

where

$$(A4) \quad v = ka \cos \tilde{\gamma} = k\rho \cos \gamma,$$

and the contour of integration,  $C_v$ , is indicated below in Fig. A-I. Also,  $\psi = (|\phi| - \pi/2)$  as before.

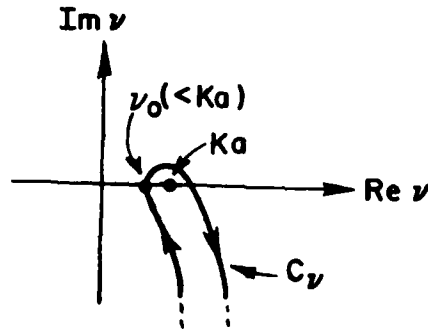


Fig. A-I. Contour of integration  $C_v$ .

Rewriting the integral in (A3) as

$$(A5) \quad U_r \sim - \sqrt{\frac{1}{2\pi k}} e^{-i\frac{\pi}{4}} \int_{C_v} \frac{e^{ikf(v)}}{\sqrt{\rho \sin \gamma}} dv$$

where

$$(A6) \quad f(v) \equiv 2a \sin \tilde{\gamma} - \left( \frac{2v}{k} \tilde{\gamma} \right) - \rho \sin \gamma + \frac{v}{k} \gamma - \frac{v}{k} \psi,$$

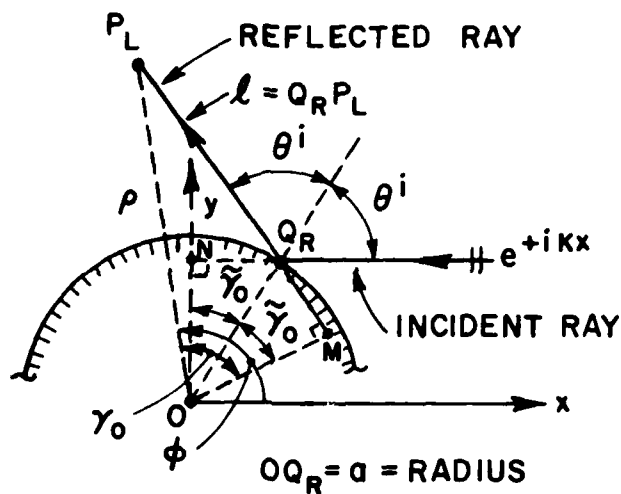
one obtains the following saddle point ( $v = v_0$ ) condition:

$$(A7) \quad \left. \frac{\partial f}{\partial v} \right|_{v=v_0} = 0 ; \quad \psi = \gamma_0 - 2 \tilde{\gamma}_0, \quad \left( \begin{array}{l} \gamma = \gamma_0 \text{ at } v = v_0 \\ \tilde{\gamma} = \tilde{\gamma}_0 \text{ at } v = v_0 \end{array} \right).$$



$$(A8) \quad \cos \theta^i = \sin \gamma_0^i, \quad \text{when } v = v_0, \quad$$

$$(A9) \quad \rho \sin \gamma \Big|_{v=v_0} = \rho \sin \gamma_0 = \ell + a \sin \tilde{\gamma}_0 = \ell + a \cos \theta^i.$$



The geometrical significance of (A7), (A8), and (A9) is shown in Fig. A-II. Also,

$$\begin{aligned} f(v_0) &= a \cos \theta^i - \ell \\ f'(v_0) &= 0 \end{aligned}$$

$$f''(v_0) = \frac{2 \ell + a \cos \theta^i}{(ka \cos \theta^i)(k\rho \sin \gamma_0)},$$

62

Incorporating the above expressions into the saddle point result for (A5) gives

$$(A10) \quad U_r \sim -\sqrt{\frac{1}{2\pi}} e^{-i\frac{\pi}{4}} \sqrt{\frac{-2\pi}{ikf''(v_0)}} \frac{e^{ikf(v_0)}}{\sqrt{k\rho \sin \gamma_0}} .$$

One finally obtains

$$(A11) \quad U_r \sim -e^{ika \cos \theta^i} \cdot \sqrt{\frac{\frac{a \cos \theta^i}{2}}{\frac{a \cos \theta^i}{2} + \ell}} e^{-ik\ell}, \text{ for TM}_Z \text{ case;}$$

which in the notation of section II B reduces to

$$(A12) \quad U_r \sim R_{sh} \cdot U^i(Q_R) \sqrt{\frac{\rho_r}{\rho_r + \ell}} e^{-ik\ell}; \quad R_{sh} = \begin{cases} \mp 1; & \text{TM}_Z \\ & \text{TE}_Z \end{cases} ,$$

which is the required reflected geometrical optics field.